International Journal of Plasticity 139 (2021) 102957

Contents lists available at ScienceDirect

International Journal of Plasticity

journal homepage: http://www.elsevier.com/locate/ijplas

A finite strain thermomechanically-coupled constitutive model for phase transformation and (transformation-induced) plastic deformation in NiTi single crystals

M.A. Hossain, Th. Baxevanis *

Department of Mechanical Engineering, University of Houston, Houston, TX, 77204-4006, USA

ARTICLE INFO

Keywords:
NiTi
Transformation-induced plasticity
Phase transformation
Latent heat effects
Shape memory alloys

ABSTRACT

A 3D finite-strain constitutive model for the deformation response of NiTi at the single crystal level is proposed. The model accounts for reversible phase transformation from austenite to martensite habit plane variants, plastic deformation in the austenite phase, and rate effects induced from latent heat. It is developed within the formalism of irreversible thermodynamics with internal state variables based on the Eulerian logarithmic strain and its corrotational objective rate. The inelastic deformation is defined as an average over a representative volume element as classical in the micromechanics-based modeling approach. Transformation-induced plastic deformation is viewed as a mechanism for accommodation of the local deformation incompatibility at the austenite–martensite interface. It is accounted for by introducing an interaction term in the free energy, which is described through the Eshelby tensor by regarding the habit plane variants as ellipsoidal inclusions embedded in the austenite matrix, in order to accurately reflect the internal stress states that contribute to dislocation slipping. The numerical implementation of the model in an efficient scheme and its calibration are described in detail. The proposed model is validated by comparing simulations with available experimental data in single NiTi crystals. Numerical simulations of polycrystals are performed to obtain an insight into the interaction between phase transformation and plastic deformation induced by intergrannular constraints. The efficiency of the numerical implementation of the model is verified by simulations of indentation tests.

1. Introduction

Shape Memory Alloys (SMAs) exhibit a reversible, solid-to-solid, phase transformation from austenite to martensite. High inelastic strains, induced during forward phase transformation from austenite to martensite, can be recovered during reverse phase transformation, rendering these materials highly desirable in engineering applications (Miyazaki, 1990; Otsuka and Wayman, 1999; Morgan, 2004; Lagoudas, 2008; Jani et al., 2014; Barbarino et al., 2014). NiTi is the most widely used/studied SMA due to its excellent mechanical properties, good processability, corrosion and wear resistance, and biocompatibility.

In NiTi, austenite, which is characterized by a cubic B2 crystallographic structure, transforms into 12 monoclinic martensite variants (B19' crystallographic structure) by mechanical loading and/or cooling, during which chemical composition remains

* Corresponding author.
E-mail addresses: afzalhossain7.bd@gmail.com (M.A. Hossain), tbaxevanis@uh.edu (Th. Baxevanis).

https://doi.org/10.1016/j.ijplas.2021.102957
Received 18 November 2020; Received in revised form 29 January 2021; Accepted 12 February 2021
Available online 23 February 2021

unaltered while the atoms are organized in a new crystallographic lattice (non-diffusive, first-order phase transition). The martensite phase is formed as thin platelets, needles, or laths within the austenite parent phase with the two phases fitting together along planes, called *invariant* or *habit* planes, that remain unchanged, *i.e.*, neither deform nor rotate. These planes/interfaces are between austenite and twins of martenite variants, called *Habit Plane Variants* (HPVs), that comprise of two *Lattice Correspondent Variants* (LCVs). Crystallographic theory predicts 192 HPVs, *i.e.*, 192 possible distinct interfaces between austenite and martensite (Hane and Shield, 1999). Movement of interfaces between HPVs is referred to as HPV *reorientation*, and movement of interfaces between LCVs as *detwinning*.

Phase transformation is accompanied by irrecoverable strain that accumulates with cycling (Miyazaki et al., 1986; Eggeler et al., 2004; Nemat-Nasser and Guo, 2006; Zaki and Moumni, 2007; Norfleet et al., 2009; Kang et al., 2009, 2012; Delville et al., 2010; Manchiraju et al., 2011; Delville et al., 2011; Morin et al., 2011a,b; Sun et al., 2012; Yin and Sun, 2012; Yin et al., 2014; Song et al., 2014; Benafan et al., 2014). The residual strain is due to dislocation slipping in austenite phase (and deformation twinning in martensite at higher load levels) (Miyazaki et al., 1986; Hamilton et al., 2004; Norfleet et al., 2009; Delville et al., 2010, 2011; Simon et al., 2010; Pelton et al., 2012; Pfetzing-Micklich et al., 2012; Benafan et al., 2013, 2014) and residual martensite due to incomplete reverse phase transformation (Miyazaki et al., 1986; Brinson et al., 2004). In the single crystal level, the accumulated residual strain is characterized by strong anisotropy, *i.e.*, depends greatly on crystallographic orientation, and precipitates. In solution heat-treated, precipitation-free, single crystals, most of the irrecoverable strain is due to dislocation slipping while in the high-resistant against dislocation activity nano-sized precipitated single crystals is mainly due to residual martensite (Gall et al., 2001, 2002; Gall and Maier, 2002). Plastic deformation in austenite is influenced by $\langle 100\rangle\{011\}$ and $\langle 101\rangle\{001\}$ slip modes (Chumlyakov et al., 1996) and, as recently observed, by $\langle 111\rangle\{110\}$ (Ezaz et al., 2013). The plastic deformation in martensite is mainly due to twin activity, 11 possible twinning systems were pointed out by Otsuka and Ren (2005), while only one slip system (001)[100] exists due to the low symmetry of the martensite monoclinic crystal structure. Dislocation slipping is observed even if the overall applied stress is lower than the yield stress of austenite as a mechanism to accommodate the deformation incompatibility at the austenite–martensite interfaces (Norfleet et al., 2009; Simon et al., 2010), thus termed TRansformation-Induced Plasticity (TRIP). The phase transformation–plasticity coupling results in undesirable characteristics such as reduced work output (functional fatigue) and early fatigue failure (structural fatigue) during repeated thermomechanical cycling.

A variety of *micromechanics-based* models have been developed that simulate the various deformation mechanisms in NiTi at the single crystal level (Patoor et al., 1996, 2006; Huang et al., 2000; Gall et al., 2000; Gao et al., 2000; Thamburaja and Anand, 2001, 2002; Anand and Gurtin, 2003; Thamburaja, 2005; Wang et al., 2008; Thamburaja and Nikabdullah, 2009; Manchiraju and Anderson, 2010; Yu et al., 2015b). Most of the early models capture only forward and reverse phase transformation. Subsequently, models have been developed for reorientation of HPVs, detwinning of LCVs, dislocation slipping and deformation twinning. A summary of these models can be found in Dhala et al. (2019). Micromechanics-based models are (i) easily implementable in numerical methods for the full-field solution of boundary value problems in polycrystalline settings where misorientation across grains, grain boundaries, and triple joints can give rise to complex stress states, and (ii) are amenable to mean-field scale translation rules (*e.g.*, Mori-Tanaka and self-consistent approaches). The existing micromechanics-based models that describe both phase transformation and plastic deformation, with the exception of Cherkaoui et al. (1998) and Yu et al. (2015a), cannot effectively describe TRIP since they do not explicitly account for the local rise of internal stress near the austenite–martensite interfaces. Furthermore, the existing models, with the exception of Yu et al. (2015b) and Xiao et al. (2018), are isothermal, an assumption valid only for a range of strain rates within the regime of quasi-static processes. At higher strain rates, the generation or absorption of latent heat may have a strong impact on the deformation response of NiTi (Leo et al., 1993; McCormick et al., 1993; Shaw and Kyriakides, 1995; Prahlad and Chopra, 2003; Eggeler et al., 2004; Morin et al., 2011c; He and Sun, 2011).

The aim of the present paper is the development of a 3D, micromechanics-based, single crystal model to describe the deformation response of NiTi, including a description of TRIP as a mechanism for accommodation of the deformation incompatibility at the austenite–martensite interface, which allows for finite deformations and thermally-induced rate effects within a consistent thermodynamic framework. The model accounts for reversible phase transformation from austenite to HPVs and dislocation slipping in the austenite state, neglecting reorientation of HPVs, detwinning of LCVs, and deformation twinning in martensite. Thus, the model targets superelasticity and shape memory effect for coupled thermo-mechanical, nearly proportional, loading within a range that does not allow for considerable martensite plastic deformation or formation of self-accommodated martensite. The interaction between the two phases is described through the Eshelby tensor by regarding the HPVs as ellipsoidal inclusions embedded in the austenite matrix in order to reflect the internal stress states that can activate dislocation slipping even for applied load levels that could not otherwise (Cherkaoui et al., 1998; Yu et al., 2015a).

Contrarily to the finite-strain, single crystal NiTi models that are all based on the multiplicative decomposition of the deformation gradient into elastic and inelastic parts (Anand and Gurtin, 2003; Thamburaja and Anand, 2001, 2002; Thamburaja, 2005; Manchiraju and Anderson, 2010; Paranjape et al., 2016), the present model is based on an additive decomposition of the rate of deformation, and, thus, achieves a simpler model structure and an easier implementation procedure. Infinitesimal-strain model formulations are known to overestimate the extend of phase transformation and predict an overly stiff rotational response (Christ and Reese, 2008; Reese and Christ, 2008). The proposed model is based on the Eulerian logarithmic strain or Hencky strain (Hencky, 1928), which is the only strain measure that its corotational rate is the rate of deformation tensor (Reinhardt and Dubey, 1995; Xiao et al., 1997), its spherical and the deviatoric parts separate the volumetric deformation and the isochoric deformation in an additive manner (Xiao et al., 2004), and satisfies the so-called Seth-Hill requirements that strain should approach $+\infty$ ($-\infty$) when the stretch approaches $+\infty$ (0) (Darijani and Naghdabadi, 2010). Other objective rates (*e.g.*, Zaremba-Jaumann-Noll rate, Green-Naghdi-Dienes rate, and Truesdell rate) combined with the Hencky or any other finite strain measure may result in spurious phenomena (*e.g.*, shear stress oscillation, artificial stress

residuals, *etc*). The proposed finite-strain model is obtained by an *ad hoc* extension of its infinitesimal-strain counterpart. A rotated constitutive description is adopted, which ensures that all "rotated objects" remain unaltered under superposed spatial rigid body motions.

The paper is organized as follows. In Section 2, the kinematics of local deformation mechanisms inside representative volume elements and their relation to the overall inelastic deformation rate is presented. The proposed model is described in Section 3 under the infinitesimal-strain assumption; the finite-strain model is obtained in the same section by an *ad hoc* extension of its infinitesimal-strain counterpart. The numerical implementation of the model in an efficient scheme is described in detail in Section 4. The model calibration and its validation against available experimental data are presented in Section 5 and numerical simulations of the deformation response of polycrystals and indentation tests in Section 6. A summary of the paper is given in Section 7.

2. Kinematics

The inelastic deformation of an SMA crystal is defined as an average over a Representative Volume Element (RVE), which should be large enough to include a sizable set of martensite HPVs and slip systems within a single crystal austenite. It is further assumed that the austenite–martensite formed interfaces are coherent and their motion along with the dislocation motion is rate-independent.

For later use, the volume fraction of martensite corresponding to the α_{th}-HPV system in an RVE is denoted as ξ^{α}, restricted by $0 \leq \xi^{\alpha} \leq 1$. The total volume fraction of martensite in a crystal, $\xi = \sum_{\alpha} \xi^{\alpha}$, must lie in the range $0 \leq \xi^{\alpha} \leq 1$.

2.1. Strain decomposition

Assuming initially infinitesimal strains, additive decomposition of the total macroscopic strain tensor, defined as the average total strain over the RVE, reads as

$$\boldsymbol{\epsilon} = \boldsymbol{\epsilon}^{e} + \boldsymbol{\epsilon}^{t} + \boldsymbol{\epsilon}^{p}, \tag{1}$$

where $\boldsymbol{\epsilon}^{e}$, $\boldsymbol{\epsilon}^{t}$, and $\boldsymbol{\epsilon}^{p}$ stand for the elastic, transformation, and plastic strain tensors, respectively. Thermal strain is an order of magnitude smaller than the transformation strain and is thus not included for simplicity. The thermal expansion of the monoclinic martensite variants is highly anisotropic (Monroe et al., 2016) and its proper implementation in a single crystal model is not trivial (Yu et al., 2019).

The finite strain extension of the model is described in Section 3.5.

2.1.1. Transformation strain

By the rule of mixtures, the transformation strain can be written as

$$\boldsymbol{\epsilon}^{t} = \sum_{\alpha=1}^{N_t} \widehat{\boldsymbol{\epsilon}}_{t}^{\alpha} \xi^{\alpha}, \tag{2}$$

where $\widehat{\boldsymbol{\epsilon}}_{t}^{\alpha} = \frac{1}{2} g_t (\boldsymbol{d}^{\alpha} \otimes \boldsymbol{l}^{\alpha} + \boldsymbol{l}^{\alpha} \otimes \boldsymbol{d}^{\alpha})$, $\boldsymbol{d}^{\alpha}$, $\boldsymbol{l}^{\alpha}$, and g_t are the stress free transformation strain, the transformation direction, the habit plane normal, and the magnitude of transformation, respectively, for each of the N_t martensite HPVs, given by crystallography.

The rate of $\boldsymbol{\epsilon}^{t}$ thus reads as

$$\dot{\boldsymbol{\epsilon}}^{t} = \sum_{\alpha=1}^{N_t} \widehat{\boldsymbol{\epsilon}}_{t}^{\alpha} \dot{\xi}^{\alpha}. \tag{3}$$

2.1.2. Plastic strain

The overall plastic strain tensor of the RVE can be written, by employing the rule of mixtures, as

$$\boldsymbol{\epsilon}^{p} = (1-\xi)\boldsymbol{\epsilon}_{A}^{p} + \sum_{\alpha=1}^{N_t} \xi^{\alpha} \boldsymbol{\epsilon}_{M_\alpha}^{p}, \tag{4}$$

where $\boldsymbol{\epsilon}_{A}^{p}$ and $\boldsymbol{\epsilon}_{M_\alpha}^{p}$ stand for the plastic strain tensors in the regions occupied by austenite and α_{th}-martensite HPV, respectively.

The rate of $\boldsymbol{\epsilon}^{p}$ is thus given as

$$\dot{\boldsymbol{\epsilon}}^{p} = (1-\xi)\dot{\boldsymbol{\epsilon}}_{A}^{p} + \sum_{\alpha=1}^{N_t} \xi^{\alpha} \dot{\boldsymbol{\epsilon}}_{M_\alpha}^{p} - \sum_{\alpha=1}^{N_t} \dot{\xi}^{\alpha} \left(\boldsymbol{\epsilon}_{A}^{p} - \boldsymbol{\epsilon}_{M_\alpha}^{p}\right) = (1-\xi)\left[\dot{\boldsymbol{\epsilon}}^{p}{}_{A} - \sum_{\alpha=1}^{N_t} \frac{\dot{\xi}^{\alpha}}{1-\xi} \left(\boldsymbol{\epsilon}_{A}^{p} - \boldsymbol{\epsilon}_{M_\alpha}^{p}\right)\right] + \sum_{\alpha=1}^{N_t} \xi^{\alpha} \left[\dot{\boldsymbol{\epsilon}}^{p}{}_{M_\alpha} - \frac{\dot{\xi}^{\alpha}}{\xi^{\alpha}} \left(\boldsymbol{\epsilon}_{A}^{p} - \boldsymbol{\epsilon}_{M_\alpha}^{p}\right)\right] \tag{5}$$

The rate of $\boldsymbol{\epsilon}^{p}$ can moreover be described by crystallographic slip mechanisms in the austenite phase

$$\dot{\boldsymbol{\epsilon}}^{p} = (1-\xi) \sum_{l=1}^{N_A} {}_{A}\widehat{\boldsymbol{\epsilon}}_{p}^{l} \dot{\gamma}_{A}^{l}, \tag{6}$$

where ${}_{A}\widehat{\boldsymbol{\epsilon}}_{p}^{l} = \frac{1}{2}\left(\boldsymbol{q}_{A}^{l} \otimes \boldsymbol{r}_{A}^{l} + \boldsymbol{r}_{A}^{l} \otimes \boldsymbol{q}_{A}^{l}\right)$ is the orientation tensor of the l_{th}-slipping system of austenite, $\boldsymbol{q}_{A}^{l}$, $\boldsymbol{r}_{A}^{l}$, $\dot{\gamma}_{A}^{l}$ are the respective shear

direction, slip plane normal, and average shearing rate, respectively, and N_A denotes the number of slip systems.

Combining (5) and (6), which hold for every $\xi^\alpha \in [0, 1]$, $\alpha = 1, \ldots, N_t$, yields

$$\begin{cases} \dot{\boldsymbol{\epsilon}}_A^p = \sum_{\alpha=1}^{N_t} \dfrac{\dot{\xi}^\alpha}{1-\xi}\left(\boldsymbol{\epsilon}_A^p - \boldsymbol{\epsilon}_{M_\alpha}^p\right) + \sum_{l=1}^{N_A} {}_A\widehat{\boldsymbol{\epsilon}}_p^l \dot{\gamma}_A^l, \quad \dot{\boldsymbol{\epsilon}}^p{}_{M_\alpha} = \dfrac{\dot{\xi}^\alpha}{\xi^\alpha}\left(\boldsymbol{\epsilon}_A^p - \boldsymbol{\epsilon}_{M_\alpha}^p\right) \end{cases} \tag{7}$$

Thus, the rates of plastic strain in the austenite and α_{th}-martensite HPV are dependent on the dislocation slip rates on austenite's slip systems and on the rates of expansion/shrinkage of the HPVs, thus, the model accounts for the inheritance of plastic strain from one phase to another.

3. Thermodynamics and constitutive equations

3.1. Helmholtz free energy & dissipation

Following the choice of the applied strain tensor $\boldsymbol{\epsilon}$ and absolute temperature T as external state variables, the Helmholtz free energy per unit reference volume is taken to be

$$\begin{aligned} \Phi\left(\boldsymbol{\epsilon}, T, \xi^\alpha, \gamma_A^l\right) &= \Phi_{el}\left(\boldsymbol{\epsilon}, T, \xi^\alpha, \gamma_A^l\right) + \Phi_{int}\left(\boldsymbol{\epsilon}, T, \xi^\alpha, \gamma_A^l\right) + \Phi_{ch}\left(\boldsymbol{\epsilon}, T, \xi^\alpha, \gamma_A^l\right) \\ &= \underbrace{\frac{1}{2}\boldsymbol{\epsilon}^e : \mathrm{C} : \boldsymbol{\epsilon}^e}_{\text{elastic energy}} + \underbrace{\Phi_{int}\left(\boldsymbol{\epsilon}, T, \xi^\alpha, \gamma_A^l\right)}_{\text{interaction energy}} + \underbrace{c\left[\left(T - T_0\right) - T\ln\left(\frac{T}{T_0}\right)\right] + \frac{\lambda}{T_T}(T - T_T)\xi}_{\text{chemical energy}}, \end{aligned} \tag{8}$$

where the interaction energy is defined through its rate as in Cherkaoui et al. (1998).[1]

$$\dot{\Phi}_{int} = (\mathrm{C} : \boldsymbol{\epsilon}^e) : \dot{\boldsymbol{\epsilon}}^p - \boldsymbol{\sigma}_A : (1-\xi)\sum_{l=1}^{N_A} {}_A\widehat{\boldsymbol{\epsilon}}_p^l \dot{\gamma}_A^l, \tag{9}$$

and.

$$\boldsymbol{\sigma}_A = \mathrm{C} : \boldsymbol{\epsilon}^e + \sum_{\alpha=1}^{N_t} \xi^\alpha \mathrm{C} : (\mathrm{I} - \mathrm{S}^\alpha) : \left(\widehat{\boldsymbol{\epsilon}}_t^\alpha + \boldsymbol{\epsilon}_{M_\alpha}^p - \boldsymbol{\epsilon}_A^p\right), \tag{10a}$$

$$\boldsymbol{\sigma}_{M_\alpha} = \boldsymbol{\sigma}_A - \mathrm{C} : (\mathrm{I} - \mathrm{S}^\alpha) : \left(\widehat{\boldsymbol{\epsilon}}_t^\alpha + \boldsymbol{\epsilon}_{M_\alpha}^p - \boldsymbol{\epsilon}_A^p\right) \tag{10b}$$

The model parameters C and c denote the effective stiffness tensor and specific heat at the reference state, respectively. The assumption $\mathrm{C} = \mathrm{C}_M^\alpha = \mathrm{C}_A$ is adopted for simplicity. Moreover, c is assumed to be phase-independent, which is a common engineering assumption. The parameter T_T is the phase equilibrium temperature and λ is the latent heat of transformation at temperature T_T. $\boldsymbol{\sigma}_A$ and $\boldsymbol{\sigma}_{M_\alpha}$ stand for the average stress values in the austenite and the α_{th}-martensite HPV (Cherkaoui et al., 1998), S^α stands for the Eshelby's tensor of the α_{th}-martensite HPV, which depends on the elastic constants and shape of the variant, and I is the fourth-order unit tensor.

Using the above expression of the Helmholtz free energy, the dissipation inequality (A.6) reads as

$$D = (\boldsymbol{\sigma} - \mathrm{C} : \boldsymbol{\epsilon}^e) : \dot{\boldsymbol{\epsilon}}^e + \left(s - c\ln\frac{T}{T_0} + \frac{\lambda}{T_0}\xi\right)\dot{T} + \sum_{\alpha=1}^{N_t}\left[\boldsymbol{\sigma} : \widehat{\boldsymbol{\epsilon}}_t^\alpha - \frac{\lambda}{T_T}(T - T_T)\right]\dot{\xi}^\alpha + (1-\xi)\boldsymbol{\sigma}_A : \sum_{l=1}^{N_A} {}_A\widehat{\boldsymbol{\epsilon}}_p^l \dot{\gamma}_A^l \geq 0. \tag{11}$$

The standard thermodynamical procedure, commonly referred to as the Coleman–Noll procedure (Coleman and Gurtin, 1967), applied to the dissipation inequality (11), yields the constitutive relationships.

$$\boldsymbol{\sigma} = \mathrm{C} : \boldsymbol{\epsilon}^e, \tag{12}$$

$$s = c\ln\frac{T}{T_0} - \frac{\lambda}{T_0}\xi, \tag{13}$$

Where $\boldsymbol{\sigma}$ stands for the Cauchy stress tensor, and reduces the dissipation expression to

$$D = \sum_{\alpha=1}^{N_t}\left[\boldsymbol{\sigma} : \widehat{\boldsymbol{\epsilon}}_t^\alpha - \frac{\lambda}{T_T}(T - T_T)\right]\dot{\xi}^\alpha + (1-\xi)\boldsymbol{\sigma}_A : \sum_{l=1}^{N_A} {}_A\widehat{\boldsymbol{\epsilon}}_p^l \dot{\gamma}_A^l. \tag{14}$$

[1] The derivation of the interaction term in Cherkaoui et al. (1998) is based on the Mori-Tanaka and Kröner micromechanical assumptions and the instantaneous growth hypothesis according to which the martensitic domains form instantaneously.

3.2. Driving forces

From the above dissipation expression, (14), the driving forces for phase transformation and plastic deformation can be invoked as the quasi-conservative thermodynamic forces conjugate to the respective internal variables.

Martensitic transformation.– For transformation of austenite to a particular martensite HPV, α, the driving force, F_α^t, for this HPV should satisfy the following nonequilibrium condition

$$F_t^\alpha = \boldsymbol{\sigma} : \widehat{\boldsymbol{\epsilon}}_t^\alpha - \frac{\lambda}{T_T}(T - T_T) = {}_f f_t^\alpha, \tag{15}$$

where ${}_f f_t^\alpha > 0$ is the HPV hardness, and $\boldsymbol{\sigma} : \widehat{\boldsymbol{\epsilon}}_t^\alpha$ is the resolved stress on the α_{th}-transformation system, but not in the classical Schmid sense since $\boldsymbol{l}^\alpha$ is typically not perpendicular to $\boldsymbol{d}^\alpha$.

For this particular martensite HPV to transform back to austenite, the following condition must be met

$$-F_t^\alpha = -\boldsymbol{\sigma} : \widehat{\boldsymbol{\epsilon}}_t^\alpha + \frac{\lambda}{T_T}(T - T_T) = {}_r f_t^\alpha, \tag{16}$$

where ${}_r f_t^\alpha > 0$.

Plastic deformation of austenite.– For plastic deformation of austenite, the driving force for dislocation slip of the l_{th}-slip system, ${}_A F_p^l$, should satisfy the following condition

$$\left|{}_A F_p^l\right| = \left|\left(1 - \xi\right)\boldsymbol{\sigma}_A : {}_A\widehat{\boldsymbol{\epsilon}}_p^l\right| = {}_A f_p^l, \tag{17}$$

where ${}_A f_p^l > 0$ is the respective slip system hardness.

Note that the absolute value of the resolved shear stress ${}_A F_p^l$ on the l_{th}-slip system is of interest, which explains the use of the absolute value in (16), since slip may occur in either the positive or negative direction on a slip plane, contrary to phase transformation, where the polar nature of the atomic arrangements for phase transformation requires the signed value of the resolved stress on a transformation system.

3.3. Evolution equations

The evolution laws of martensitic transformation and plastic deformation are given by the following power-law relations, in which the exponents are chosen sufficiently large to approximate rate-independent conditions.

Martensitic transformation.– The evolution law for the volume fraction of the α_{th}-martensite HPV follows the power-law relation

$$\dot{\xi}^\alpha = \begin{cases} \dot{\xi}_0 \left(\dfrac{F_t^\alpha}{{}_f f_t^\alpha}\right)^n; & F_t^\alpha > 0, \quad \text{austenite} \rightarrow \text{martensite} \\ -\dot{\xi}_0 \left(\dfrac{\left|F_t^\alpha\right|}{{}_r f_t^\alpha}\right)^n; & F_t^\alpha < 0, \quad \text{martensite} \rightarrow \text{austenite} \end{cases} \tag{18}$$

where

$$\begin{cases} {}_f f_t^\alpha = \sum_{\beta=1}^{N_t} H_t^{\alpha\beta}\xi^\beta + \xi^\alpha J_t\gamma + {}_f^c f_t^\alpha, \quad {}_r f_t^\alpha = \sum_{\beta=1}^{N_t} H_t^{\alpha\beta}\xi^\beta + (1 - \xi^\alpha)J_t\gamma + {}_r^c f_t^\alpha, \end{cases} \tag{19}$$

where $\dot{\xi}_0$ is a reference transformation strain rate, $\left[H_t^{\alpha\beta}\right]$ is the interaction energy (constant) matrix between the different martensite HPVs, the scalar $J_t > 0$ describes the increasing resistance to phase transformation due to plastic deformation, and $\gamma = \sum_{l=1}^{N_A}\left|\gamma_A^l\right|$ is the accumulated total slip. ${}_f^c f_t^\alpha$ and ${}_r^c f_t^\alpha$ are positive scalars.

Plastic deformation of austenite.– The slip rate in the l_{th}-slip system of austenite is given as

$$\dot{\gamma}_A^l = \dot{\gamma}_0 \left(\frac{{}_A F_p^l}{{}_A f_p^l}\right)\left(\frac{\left|{}_A F_p^l\right|}{{}_A f_p^l}\right)^{n-1}, \tag{20}$$

with the evolution law of the hardness, ${}_A f_p^l$, reading as

$${}_A\dot{f}_p^l = \sum_{r=1}^{N_A} {}_A H_p^{lr}\left|\dot{\gamma}_A^r\right|, \quad {}_A f_p^l(0) = {}_A^c f_p^l, \tag{21}$$

where $\dot{\gamma}_0$ is reference plastic strain rate, the matrix

$$ {}_{A}H_{p}^{lr} = {}_{A}H_{p}[q + (1-q)\delta_{lr}]\left(1 - \frac{\gamma}{\gamma_{p}^{0}}\right)^{m_{p}}, \tag{22} $$

describes the history-dependent rate of increase of the deformation resistance on slip system l due to shearing on slip system r, given in terms of the accumulated total slip, q stands for a constant latent-hardening parameter that ranges between 1 and 1.04, the positive scalar ${}_{A}H_{p}$ is the initial slip-system hardening rate, m_p is the strain hardening exponent, and δ_{lr} are the components of the Kronecker's delta, $\boldsymbol{\delta}$, *i.e.*, $\delta_{lr} = 1$ if $l = r$ and $\delta_{lr} = 0$ if $l \neq r$. ${}_{A}^{c}f_{p}^{l}$, ${}_{A}H_{p}$, m_p, and γ_{p}^{0} are positive scalars.

3.4. Thermomechanical coupling: latent-heat effects

Latent heat effects can be neglected for mechanical and thermal loading rates sufficiently slow with respect to the time rate of heat transfer by conduction/convection. Such an assumption is valid for a range of strain and thermal loading rates even for complex geometries and loadings (Prahlad and Chopra, 2003). At higher rates, though, depending on the geometry, convective boundary conditions, and associated heat transfer, the generation or absorption of latent heat may have a strong impact on the deformation response of SMAs as shown experimentally in Shaw and Kyriakides (1995); Prahlad and Chopra (2003). In those cases, latent heat effects can be taken into account as follows.

In view of (A.6), (14) can be written as

$$ D = \sum_{\alpha=1}^{N_t} F_{t}^{\alpha}\dot{\xi}^{\alpha} + \sum_{l=1}^{N_A} {}_{A}F_{p}^{l}\dot{\gamma}_{A}^{l} = \dot{s}T + \nabla\cdot\mathrm{q} - r, $$

Given the constitutive relationship (13), the entropy rate is reduced to the following explicit evaluation

$$ \dot{s} = c\frac{\dot{T}}{T} - \frac{\lambda}{T_T}\dot{\xi}, \tag{23} $$

and, thus, (23), reads as

$$ c\dot{T} - \underbrace{\sum_{\alpha=1}^{N_t}\left(F_{t}^{\alpha} + \frac{\lambda}{T_T}T\right)\dot{\xi}^{\alpha}}_{\text{heat absorbed or released during transformation}} \underbrace{-\sum_{l=1}^{N_A} {}_{A}F_{p}^{l}\dot{\gamma}_{A}^{l}}_{\text{heat released during plastic deformation}} = -\nabla\cdot\mathrm{q} + r, \tag{24} $$

which is the 3D form of the fully thermomechanically-coupled energy balance equation for SMAs.

The heat flux q at the referential state is assumed to be governed by Fourier's law

$$ \mathrm{q} = \mathrm{k}(\xi)\nabla T, \tag{25} $$

where $\mathrm{k}(\xi) = (1-\xi)\mathrm{k}_A + \sum_{\alpha=1}^{N_t}\xi^{\alpha}\mathrm{k}_M^{\alpha}$ stands for the thermal conductivity, which is approximated from the conductivities of austenite, k_A, and martensite HPVs, k_M^{α} ($\alpha = 1, \ldots N_t$), by the rule of mixtures.

3.5. Finite-strain extension of the constitutive law

The finite-strain extension of the constitutive law is based on the Eulerian logarithmic strain

$$ \mathrm{h} = \frac{1}{2}\ln\mathrm{b} = \sum_{\alpha=1}^{m}\ln\lambda^{\alpha}\mathrm{b}^{\alpha}, \tag{26} $$

introduced as the logarithmic measure of the left Cauchy-Green deformation tensor $\mathrm{b} = \mathrm{FF}^{T}$ (F is the deformation gradient, λ^{α} are the m distinct eigenvalues of b, and b^{α} are the corresponding eigenprojections) and its conjugate Kirchhoff stress

$$ \boldsymbol{\tau} = J\boldsymbol{\sigma}, \tag{27} $$

where $J = \det\mathrm{F}$ is the Jacobian of the deformation.

The Eulerian logarithmic strain is the only strain measure whose objective time rate with respect to a corrotational frame yields the total stretching (or rate of deformation) $\mathrm{D} = \frac{1}{2}\left(\nabla\boldsymbol{v} + \nabla\boldsymbol{v}^{T}\right)$, where $\boldsymbol{v}$ stands for the velocity and the superscript ^{T} denotes transpose, *i.e.*,

$$ \overset{\circ}{\mathrm{h}} = \mathrm{D}, \tag{28} $$

where the superscript "$\circ$" denotes the objective logarithmic time rate of any Eulerian symmetric second-order tensor $\boldsymbol{a}$

$$ \overset{\circ}{\boldsymbol{a}} = \dot{\boldsymbol{a}} + \boldsymbol{a}\boldsymbol{\Omega}^{L} - \boldsymbol{\Omega}^{L}\boldsymbol{a}, \tag{29} $$

defined by the logarithmic spin $\boldsymbol{\Omega}^L = \mathrm{W} + \sum_{\alpha\neq\beta}^{n}\left(\frac{1+(\lambda^\alpha/\lambda^\beta)}{1-(\lambda^\alpha/\lambda^\beta)} + \frac{2}{\ln(\lambda^\alpha/\lambda^\beta)}\right)\mathrm{b}^\alpha\mathrm{D}\mathrm{b}^\beta$ (W is the spin tensor), and the superscript "$\cdot$" denotes material time rate.

On account of (29), relation

$$\dot{\mathrm{R}}^{L^T}\boldsymbol{a}\mathrm{R}^L = \mathrm{R}^{L^T}\dot{\boldsymbol{a}}\mathrm{R}^L, \tag{30}$$

holds, where the logarithmic rotation, R^L, is defined from the differential equation

$$\dot{R}^L = \boldsymbol{\Omega}^L\mathrm{R}^L, \quad \mathrm{R}^L|_{t=0} = \boldsymbol{\delta}. \tag{31}$$

The left hand side of (30) represents the material time rate of a Lagrangian quantity and, thus, (31) generates a one-parameter subgroup of rotations that define a locally rotating coordinate system in which the material time rates of the obtained rotated tensors remain unaltered by superposed spatial rigid body motions (Xiao et al., 1996). Time integration of (30), assuming $\boldsymbol{a} = \mathrm{h}$ and $\mathrm{h}|_{t=0} = 0$, yields

$$\mathrm{h} = \mathrm{R}^L\left(\int_0^t \mathrm{R}^{L^T}\dot{\mathrm{h}}\mathrm{R}^L\mathrm{d}t\right)\mathrm{R}^{L^T} \overset{(28)}{=} \mathrm{R}^L\left(\int_0^t \mathrm{R}^{L^T}\mathrm{D}\mathrm{R}^L\mathrm{d}t\right)\mathrm{R}^{L^T}, \tag{32}$$

and, thus, additive decomposition of total stretching D into elastic, transformation, and plastic deformation parts yields an additive decomposition of the Hencky strain

$$\mathrm{h} = \mathrm{h}^e + \mathrm{h}^t + \mathrm{h}^p. \tag{33}$$

The above additive decomposition of the Hencky strain together with (30) allows for extending the constitutive relations of *initially isotropic* materials from infinitesimal to finite deformations by simply restating them in a rotated (local) description, *i.e.*, by replacing in all relations the infinitesimal strain $\boldsymbol{\epsilon}$ by the rotated Hencky strain, $\mathrm{R}^{L^T}\mathrm{h}\mathrm{R}^L$, the Cauchy stress, $\boldsymbol{\sigma}$, by the rotated Kirchhoff stress, $\mathrm{R}^{L^T}\boldsymbol{\tau}\mathrm{R}^L$, and the material time rate of any tensorial quantity by their rotated logarithmic rate.[2] Note that in the finite strain formulation the lattice vectors $\boldsymbol{d}^\alpha$, $\boldsymbol{l}^\alpha$ ($\alpha = 1, 2 \ldots N_t$), $\boldsymbol{q}_A^l$, and $\boldsymbol{r}_A^l$ ($l = 1, 2 \ldots N_A$) are stretched and rotated as $\mathrm{F}^e\boldsymbol{d}^\alpha$, $\boldsymbol{l}^\alpha\mathrm{F}^{e-1}$, $\mathrm{F}^e\boldsymbol{q}_A^l$, and $\boldsymbol{r}_A^l\mathrm{F}^{e-1}$, respectively, where $\mathrm{F}^e = \mathrm{V}^e\mathrm{R}^e$ is the elastic part of the deformation gradient, V^e is the elastic stretch tensor determined as

$$\mathrm{V}^e = \exp(\mathrm{h}^e), \tag{34}$$

and the elastic rotation R^e is obtained by integrating the linear tensorial differential equation

$$\dot{\mathrm{R}}^e = \boldsymbol{\Omega}^e\mathrm{R}^e, \quad \mathrm{R}^e|_{t=0} = \boldsymbol{\delta}, \tag{35}$$

with $\boldsymbol{\Omega}^e = \boldsymbol{\Omega}^L - \sum_{\alpha\neq\beta}^{n}\left(\frac{2\lambda_e^\alpha\lambda_e^\beta}{\lambda_e^{\alpha 2}-\lambda_e^{\beta 2}} + \frac{1}{\ln\frac{\lambda_e^\alpha}{\lambda_e^\beta}-\ln\frac{\lambda_e^\beta}{\lambda_e^\beta}}\right)\mathrm{V}_\alpha^e\mathrm{D}^e\mathrm{V}_\beta^e$ (λ_e^α are the m distinct eigenvalues of V^e, V_α^e are the corresponding eigenprojections, and $\mathrm{D}^e = \dot{\mathrm{h}}^e$ is the elastic stretching) (Xiao et al., 2000).

An analogous extension of the constitutive relations from infinitesimal to finite deformations for initially anisotropic materials, athough possible in terms of invariance under the logarithmic rotation-conjugate group of the initial material symmetry group, is more involved and not undertaken herein (Bruhns et al., 2003). Rather, the stiffness tensors of austenite and martensite, C_A and C_M, respectively, are assumed isotropic instead, equal to $\mathrm{C}_\alpha^{iso} \equiv (\mathrm{C}_\alpha :: \mathrm{I}_V)\mathrm{I}_V + \frac{1}{5}(\mathrm{C}_\alpha :: \mathrm{I}_D)\mathrm{I}_D$, where $\mathrm{I}_V = \frac{1}{3}\boldsymbol{\delta}\otimes\boldsymbol{\delta}$ and $\mathrm{I}_D = \mathrm{I}_s - \mathrm{I}_V$ are the volumetric and deviatoric projection tensors, respectively, I_s designates the fourth-order tensor with components $I^s_{ijkl} = \frac{1}{2}\left(\delta_{ik}\delta_{jl} + \delta_{il}\delta_{jk}\right)$, A: B $= A_{ijkl}B_{lkji}$ for any fourth order tensors A, and B, and the subscript $_\alpha$ stands for $_A$ or $_M$ (Bornert et al., 2001).

The numerical implementation of the resulting model is explained in detail in Section 4.2.

4. Numerical implementation

4.1. Numerical scheme for the integration of the constitutive response

An explicit numerical integration method is employed for estimating the change in martensite volume fractions, $\Delta\xi^\alpha$, and shear rates, $\Delta\gamma_A^l$, during the current time increment, t. This method leads to improved numerical stability by resulting in a tangent stiffness expression which is considerably reduced from the elastic stiffness; in explicit integration, the maximum allowable time step is inversely related to the relevant material stiffness (Cormeau, 1975). This numerical procedure falls into the class of forward gradient

[2] Cherkaoui et al. (1998) work that motivated the interaction term in (8) is based on the Kröner (1961) and Mori and Tanaka (1973) methods under the infinitesimal-strain assumption. The proposed finite-strain extension of (8) and the resulting expressions (10) on the basis of rotated logarithmic strain and rotated Kirchhoff stress is in general an approximation that assumes all phase rotations to be equal, *i.e.*, the matrix rotation is assumed to be fully conveyed to the embedded phases.

methods and has been discussed in Peirce et al. (1984).

The increments of martensite volume fractions and slip on the slip systems of austenite at time t are given as

$$\begin{cases} \Delta\xi^{\alpha} = \xi^{\alpha}_{t+\Delta t} - \xi^{\alpha}_{t}, \\ \Delta\gamma^{l}_{A} = \left(\gamma^{l}_{A}\right)_{t+\Delta t} - \left(\gamma^{l}_{A}\right)_{t}. \end{cases} \tag{36}$$

Linear interpolation within the time increment gives

$$\begin{cases} \Delta\xi^{\alpha} = \left[(1-\theta)\dot{\xi}^{\alpha}_{t} + \theta\dot{\xi}^{\alpha}_{t+\Delta t}\right]\Delta t, \quad \Delta\gamma^{l}_{A} = \left[\left(1-\theta\right)\left(\dot{\gamma}^{l}_{A}\right)_{t} + \theta\left(\dot{\gamma}^{l}_{A}\right)_{t+\Delta t}\right]\Delta t, \end{cases} \tag{37}$$

where the parameter θ ranges from 0 to 1; $\theta = 0$ corresponds to the simplest Euler integration procedure. Taylor expansion of the last terms in the above equations yields

$$\begin{cases} \dot{\xi}^{\alpha}_{t+\Delta t} = \dot{\xi}^{\alpha}_{t} + \partial\frac{\dot{\xi}^{\alpha}_{t}}{\partial F^{\alpha}_{t}{}_{t}}\Delta F^{\alpha}_{t} + \partial\frac{\dot{\xi}^{\alpha}_{t}}{\partial f^{\alpha}_{t}{}_{t}}\Delta f^{\alpha}_{t}, \quad \left(\dot{\gamma}^{l}_{A}\right)_{t+\Delta t} = \left(\dot{\gamma}^{l}_{A}\right)_{t} + \partial\left(\frac{\dot{\gamma}^{l}_{A}\right)_{t}}{\partial_{A}F^{l}_{p}{}_{t}}\Delta_{A}F^{l}_{p} + \partial\left(\frac{\dot{\gamma}^{l}_{A}\right)_{t}}{\partial_{A}f^{l}_{p}{}_{t}}\Delta_{A}f^{l}_{p}, \end{cases}$$

which in view of the evolution equations reads as

$$\begin{cases} \dot{\xi}^{\alpha}_{t+\Delta t} = \dot{\xi}^{\alpha}_{t}\left[1 + n\left(\frac{\Delta F^{\alpha}_{t}}{F^{\alpha}_{t}} - \frac{\Delta f^{\alpha}_{t}}{f^{\alpha}_{t}}\right)\right], \quad \left(\dot{\gamma}^{l}_{A}\right)_{t+\Delta t} = \left(\dot{\gamma}^{l}_{A}\right)_{t}\left[1 + n\left(\frac{\Delta_{A}F^{l}_{p}}{{}_{A}F^{l}_{p}} - \frac{\Delta_{A}f^{l}_{p}}{{}_{A}f^{l}_{p}}\right)\right] \end{cases} \tag{38}$$

Combining (37), (38), yields

$$\begin{cases} \Delta\xi^{\alpha} = \dot{\xi}^{\alpha}_{t}\left[1 + \theta n\left(\frac{\Delta F^{\alpha}_{t}}{F^{\alpha}_{t}} - \frac{\Delta f^{\alpha}_{t}}{f^{\alpha}_{t}}\right)\right]\Delta t, \quad \Delta\gamma^{l}_{A} = \left(\dot{\gamma}^{l}_{A}\right)_{t}\left[1 + \theta n\left(\frac{\Delta_{A}F^{l}_{p}}{{}_{A}f^{l}_{p}} - \frac{\Delta_{A}f^{l}_{p}}{{}_{A}f^{l}_{p}}\right)\right]\Delta t. \end{cases} \tag{39}$$

(39) is actually of system of equations for the unknowns $\Delta\xi^{\alpha}$ and $\Delta\gamma^{l}_{A}$, which is consistent, *i.e.*, can be solved, for small time steps.

4.2. Incrementally objective time-stepping algorithm for the finite strain model

As described in Section 3.5, a rotated description of the constitutive equations is adopted for the finite extension of the infinitesimal-strain model. In view of (30), the numerical integration scheme outlined in Section 4.1 for infinitesimal strains can be followed by replacing all tensorial state variables, $\boldsymbol{\alpha}_t$, with $\mathrm{R}^{L}_{t}{}^{T}\boldsymbol{\alpha}_t\mathrm{R}^{L}_{t}$ and, $\boldsymbol{\alpha}_{t+\Delta t}$, with $\mathrm{R}^{L}_{t+\Delta t}{}^{T}\boldsymbol{\alpha}_{t+\Delta t}\mathrm{R}^{L}_{t+\Delta t}$ and assuming that the lattice vectors are constant during each increment, equal to $\mathrm{F}^{e}_{t}\boldsymbol{d}^{\alpha}$, $\boldsymbol{l}^{\alpha}\mathrm{F}^{e-1}_{t}$, $\mathrm{F}^{e}_{t}\boldsymbol{q}^{l}_{A}$, and $\boldsymbol{r}^{l}_{A}\mathrm{F}^{e-1}_{t}$.

4.2.1. Closed-form algorithm for updating the rotation tensor R^L

To update the logarithmic rate, $\mathrm{R}^{L}_{t+\Delta t}$, the deformation gradient

$$\mathrm{F}_{t+\Delta t} = (\boldsymbol{\delta} + \nabla_t[\boldsymbol{\Delta u}])\mathrm{F}_t, \quad \text{where} \quad \nabla_t[\boldsymbol{u}] = \frac{\partial \boldsymbol{u}(\boldsymbol{x}_t)}{\partial \boldsymbol{x}_t},$$

the stretching

$$\mathrm{D}_{t+\Delta t} = \frac{1}{2}\left[\frac{\mathrm{F}_{t+\Delta t} - \mathrm{F}_t}{\Delta t}\mathrm{F}^{-1}_{t+\Delta t} + \left(\frac{\mathrm{F}_{t+\Delta t} - \mathrm{F}_t}{\Delta t}\mathrm{F}^{-1}_{t+\Delta t}\right)^{T}\right],$$

and the spin

$$\mathrm{W}_{t+\Delta t} = \frac{1}{2}\left[\frac{\mathrm{F}_{t+\Delta t} - \mathrm{F}_t}{\Delta t}\mathrm{F}^{-1}_{t+\Delta t} - \left(\frac{\mathrm{F}_{t+\Delta t} - \mathrm{F}_t}{\Delta t}\mathrm{F}^{-1}_{t+\Delta t}\right)^{T}\right],$$

are first updated sequentially. Then the eigenvalues, $\lambda^{\alpha}_{t+\Delta t}$, of $\mathrm{b}_{t+\Delta t} = \mathrm{F}_{t+\Delta t}\mathrm{F}^{T}_{t+\Delta t}$ and their corresponding eigenvectors, $\mathrm{b}^{\alpha}_{t+\Delta t}$, are calculated in closed form, the former according to well-known formulas (see, *e.g.*, Malvern (1998), pp. 91–92) and the latter from Sylvester's formula

$$\mathrm{b}^{\alpha}_{t+\Delta t} = \delta_{1m}\boldsymbol{\delta} + \prod_{\beta\neq\alpha}^{m} \frac{\mathrm{b}_{t+\Delta t} - \lambda^{\beta}_{t+\Delta t}\boldsymbol{\delta}}{\lambda^{\alpha}_{t+\Delta t} - \lambda^{\beta}_{t+\Delta t}},$$

where m represents the number of distinct eigenvalues, and in turn the logarithmic rate

$$\boldsymbol{\Omega}^{L}_{t+\Delta t}\Delta t = \left[\mathrm{W}_{t+\Delta t} + \sum_{\alpha\neq\beta}^{m}\left(\frac{1+(\lambda^{\alpha}_{t+\Delta t}/\lambda^{\beta}_{t+\Delta t})}{1-(\lambda^{\alpha}_{t+\Delta t}/\lambda^{\beta}_{t+\Delta t})} + \frac{2}{\ln(\lambda^{\alpha}_{t+\Delta t}/\lambda^{\beta}_{t+\Delta t})}\right)\mathrm{b}^{\alpha}_{t+\Delta t}\mathrm{D}_{t+\Delta t}\mathrm{b}^{\beta}_{t+\Delta t}\right]\Delta t,$$

and the logarithmic rotation (see (31))

$$\mathrm{R}^{L}_{t+\Delta t} = \exp[\boldsymbol{\Omega}^{L}_{t+\Delta t}\Delta t]\mathrm{R}^{L}_{t},$$

are updated.

The exponential map, $\exp[\boldsymbol{\Omega}^{L}_{t+\Delta t}\Delta t]$, is derived in closed form as in Simo and Hughes (1998) (pp. 297),

$$\exp[\boldsymbol{\Omega}^{L}_{t+\Delta t}\Delta t] = 2\begin{bmatrix} \left(q^{0}_{t+\Delta t}\right)^{2} + \left(q^{1}_{t+\Delta t}\right)^{2} - \frac{1}{2} & q^{1}_{t+\Delta t}q^{2}_{t+\Delta t} - q^{3}_{t+\Delta t}q^{0}_{t+\Delta t} & q^{1}_{t+\Delta t}q^{3}_{t+\Delta t} + q^{2}_{t+\Delta t}q^{0}_{t+\Delta t} \\ q^{2}_{t+\Delta t}q^{1}_{t+\Delta t} + q^{3}_{t+\Delta t}q^{0}_{t+\Delta t} & \left(q^{0}_{t+\Delta t}\right)^{2} + \left(q^{2}_{t+\Delta t}\right)^{2} - \frac{1}{2} & q^{2}_{t+\Delta t}q^{3}_{t+\Delta t} - q^{1}_{t+\Delta t}q^{0}_{t+\Delta t} \\ q^{3}_{t+\Delta t}q^{1}_{t+\Delta t} - q^{2}_{t+\Delta t}q^{0}_{t+\Delta t} & q^{3}_{t+\Delta t}q^{2}_{t+\Delta t} + q^{1}_{t+\Delta t}q^{0}_{t+\Delta t} & \left(q^{0}_{t+\Delta t}\right)^{2} + \left(q^{3}_{t+\Delta t}\right)^{2} - \frac{1}{2} \end{bmatrix}$$

where $q^{0}_{t+\Delta t} = \cos(\| \boldsymbol{\omega}^{L}_{t+\Delta t} \| /2)$, $q^{i}_{t+\Delta t} = q^{*}_{t+\Delta t}\omega^{L}{}^{i}_{t+\Delta t}$, $\omega^{L}{}^{i}_{t+\Delta t} = -\frac{1}{2}\epsilon_{ijk}\Omega^{L}{}^{jk}_{t+\Delta t}\Delta t$ ($i = 1, 2, 3$) are the components of the axial (or dual) vector $\boldsymbol{\omega}^{L}_{t+\Delta t}$ of $\boldsymbol{\omega}^{L}_{t+\Delta t}\Delta t$ (ϵ_{ijk} is the permutation tensor), and

$$q^{*}_{t+\Delta t} = \begin{cases} \frac{1}{2}\dfrac{\sin(\| \boldsymbol{\omega}^{L}_{t+\Delta t} \| /2)}{\| \boldsymbol{\omega}^{L}_{t+\Delta t} \| /2}, & \left|\sin(\| \boldsymbol{\omega}^{L}_{t+\Delta t} \| /2)\right| > \mathrm{tol}. \\ \frac{1}{2}\left[1 - \| \boldsymbol{\omega}^{L}_{t+\Delta t}\|^{2}/24 + \| \boldsymbol{\omega}^{L}_{t+\Delta t}\|^{4}/1920 + \ldots\right], & \text{else}. \end{cases}$$

4.2.2. Closed-form algorithm for updating F^e

F^{e} is updated at the end of the increment similarly to the updating of R^{L} once the elastic strain h^{e}_{t+1} is calculated. The exponential map $\mathrm{V}^{e} = \exp(\mathrm{h}^{e})$ is approximated as $\mathrm{V}^{e} = \mathrm{I} + \mathrm{h}^{e}$.

4.3. Further details on the solution scheme

The Eshelby tensor is assumed identical for all HPVs and corresponds to oblate spheroids in an isotropic matrix obtained by the isotropization described at the end of Section 3.5. The lengths of the semi-axes of the ellipsoidal HPV inclusions are set as $a_1 = a_2 = a$, $a_3 = a/b$, for $b > 1$. In the simulations that follow, b is assumed equal to 4.

5. Model calibration and validation

The calibration of the proposed model, based on the experimentally determined deformation response of the material under *uniaxial loading* at various orientations, is described in this section. In the case of finite strains, experimental evaluation of the onset of phase transformation and post-transformation stress-strain behavior generally should be based on either the 1st Piola-Kirchhoff or Cauchy stress, *i.e.*, either on the undeformed or deformed configuration, respectively. However, since elastic and transformation-induced *volumetric* deformations in SMAs are small, the Kirchhoff stress, $\boldsymbol{\tau} = J\boldsymbol{\sigma} \sim \boldsymbol{\sigma}$, may be used instead of the Cauchy stress. Thus, the calibration procedure of the finite- and infinitesimal-strain models differ only on the experimental evaluation of the logarithmic strain in the former instead of the engineering strain in the latter.

Thermoelastic parameters.– The B2 structure belongs to the cubic crystal system and thus the elastic tensor of austenite phase in NiTi SMA single crystals possesses three independent constants, *i.e.*, $C^{A}_{11} = 130$ GPa, $C^{A}_{22} = 98$ GPa, and $C^{A}_{44} = 34$ GPa (Brill et al., 1991). As already mentioned, the assumption that $\mathrm{C}^{\alpha}_{M} = \mathrm{C}_{A}$ is adopted for simplicity. The thermal conductivity of the B2 austenite is isotropic, $\mathrm{k}_{A} = k_{A}\boldsymbol{\delta}$, where $k_A = 18$ W/(m K). In the absence of thermal conductivity measurements at the lattice level, the thermal conductivity of the monoclinic martensite variants although anisotropic is approximated as isotropic, $\mathrm{k}^{\alpha}_{M} \equiv k_{M}\boldsymbol{\delta}$ ($\alpha = 1, \ldots, N_l$), where $k_M = 8.6$ W/(m K). The specific heat is taken as $c = 837$ J/(kg K). These parameter values are given in Müller and Bruhns (2006).

Transformation parameters.– The transformation parameters are determined from the experiments of Gall et al. (2002) for $Ni_{50.9}Ti$

Table 1
Model parameter values. The crystallographic data for the 24 martensite HPVs in NiTi is given in Table 2 and $g_t = 0.1308$. The strain rate exponent n is set to a high value, $n = 50$.

(a) Thermoelastic Parameters		
	parameter	value
Austenite	initial density ρ_0 [g/(cm)^3]	6.45
	specific heat c [MJ/(m^3 K)]	2.1
	elastic constant C_{11}^A [GPa]	130
	elastic constant C_{22}^A [GPa]	98
	elastic constant C_{44}^A [GPa]	34
	thermal conductivity k_A [W/(m K)]	18
HPVs	elastic constants $C_M^\alpha = C_A$	
	thermal conductivity k_M [W/(m K)]	8.6
(b) Transformation Parameters		
parameter		value
equilibrium transformation temperature, T_T, [K]		257
latent heat of transformation per unit volume, λ, [MJ/m^3]		154
critical force for forward phase transformation, ${}^c_f f_t$, [MPa]		2
critical force for reverse phase transformation, ${}^c_r f_t$, [MPa]		20
hardening coefficient, J_t, [MPa]		50
(c) Austenite Plastic Deformation Parameters		
parameter		value
critical force for slip in $\langle 100\rangle\{001\}$, ${}^c_A f_p^1$, [MPa]		700
critical force for slip in $\langle 100\rangle\{011\}$, ${}^c_A f_p^2$, [MPa]		550
critical force for slip in $\langle 110\rangle\{\bar{1}11\}$, ${}^c_A f_p^3$, [MPa]		500
hardening coefficient, ${}_A H_p$, [MPa]		40
ratio of self to latent hardening, q		1.4

(at.%). T_T is calibrated from DSC measurements as $T_T = (A_s + M_s)/2 = 257$ K (Gall et al., 2002). Of the 192 possible HPVs predicted by the crystallographic theory of martensite only the 24 Type II-1 HPVs frequently observed in experiments are considered. The components of the vectors $\boldsymbol{l}^\alpha$and $\boldsymbol{d}^\alpha$ are given in Table 2 (Matsumoto et al., 1987; Gall and Sehitoglu, 1999) and $g_t = 0.1308$. The interaction matrix $\left[H_t^{\alpha\beta}\right]$, given in Siredey et al. (1999), is not accounted for since simulations showed that its inclusion overestimates the strain hardening observed in the experimental data. The latent heat is determined by referring to Manchiraju and Anderson (2010), $\lambda = 154$ MJ/m^3. The "viscous" parameter n is set to a high value, $n = 50$, to approximate the rate-independent response of NiTi. The initial critical forces for forward phase transformation are assumed identical for all martensite HPVs, ${}^c_f f_t^\alpha = {}^c_f f_t$, and, similarly ${}^c_r f_t^\alpha = {}^c_r f_t$ and $H_t^\alpha = H_t$. ${}^c_f f_t$, ${}^c_r f_t$, and H_t are evaluated by minimizing the square of the residuals between the uniaxial experimental compressive stress–strain data in Gall et al. (2002) obtained under loading in different crystallographic directions and the respective simulations as described in C.

Parameters related to TRIP.– Experimentally, only slip in the system families $\langle 100\rangle\{001\}$, $\langle 100\rangle\{011\}$, $\langle 110\rangle\{111\}$ has been observed (Ezaz et al., 2013), and, thus, only these slip families are included in the simulations. The initial critical forces for slip in these systems, ${}^c_A f_p^l$, are assumed identical for each family, and are thus reduced to ${}^c_A f_p^r$ $(r = 1, 2, 3)$. ${}^c_A f_p^r$ $(r = 1, 2, 3)$ and ${}_A H_p$ are evaluated by the least-square optimization described in C. Note that γ_p^0 and m_p in (22) cannot be reliably calibrated from the experiments reported in Gall et al. (2002) and are thus assumed null; experiments at a temperature above M_d would be required for their calibration, *i.e.*, a temperature at which stress-induced phase transformation is suppressed.

The model parameter values are given in Table 1a–c. The reference transformation rate value, $\dot{\xi}_0$, and the reference plastic strain rate, $\dot{\gamma}_0$, are representative of the applied loading rate (Beyerlein and Tomé, 2008).

5.1. Model simulations vs experimental data

In Fig. 1, simulations are compared against the experimental data used for the calibration of most of the material parameters, *i.e.*, the uniaxial compressive stress–strain curves obtained from the experiments of Gall et al. (2002) on solution heat-treated $Ni_{50.9}Ti$ (at. %) single crystals loaded along the [123], [210], [111], [211], [110] and [221] crystallographic orientations. The experimental stress–strain responses, depending on the loading orientation, differ in terms of the required load level for initiation of forward/reverse phase transformation, strain hardening, and amount of residual deformation with the simulations to reproduce quantitatively the experimental data in good agreement.

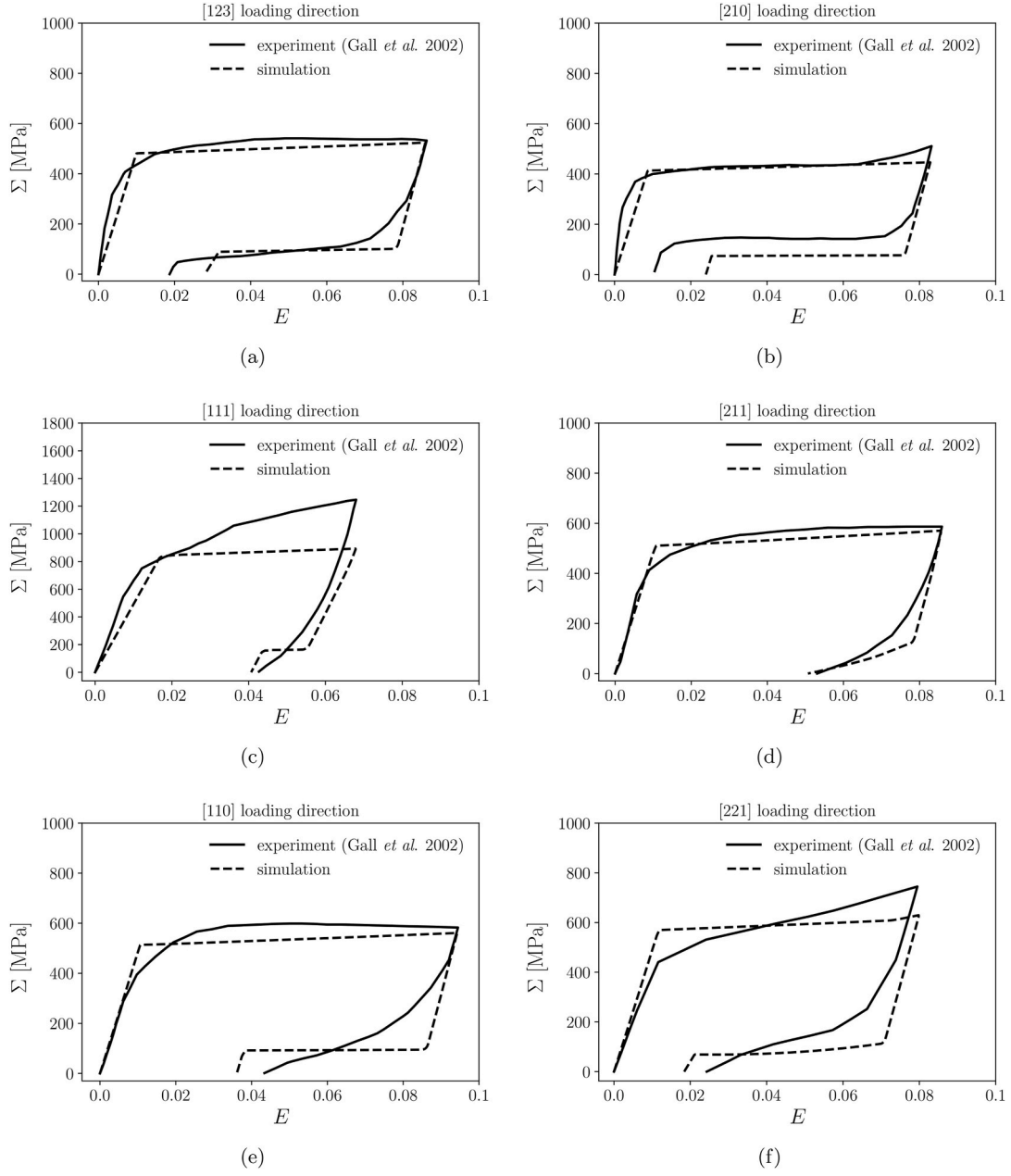

Fig. 1. Nominal stress vs engineering strain curves corresponding to uniaxial compressive loading of a single NiTi crystal along 6 different crystallographic directions. Comparison between simulations and experimental data from Gall et al. (2002).

6. Results

6.1. Simulations of the deformation response of NiTi polycrystals

The simulations presented in this section are for a polycrystalline solution heat-treated $Ni_{50.9}Ti$ (at.%) modeled in `Abaqus/Explicit®` suite by a $8 \times 8 \times 8$ cube assembly of brick elements (C3D8 for isothermal and C3D8T for thermomechanical analyses) via the finite strain version of the constitutive law. In each finite element, a single set of Euler angles is assigned, which relates the crystal basis system to the fixed global basis system, *i.e.*, each element represents a grain with an assigned crystal orientation of the austenite (B2) phase. In all simulations, random crystal orientation is imposed. Both uniaxial isothermal mechanical and isobaric thermal loading are considered. In the latter simulations, a uniaxial engineering stress, Σ, is imposed at a temperature $T = 410$ K, which is then cycled with a lower value $T = 220$ K. The upper and lower temperature were chosen such that full phase transformation takes place for

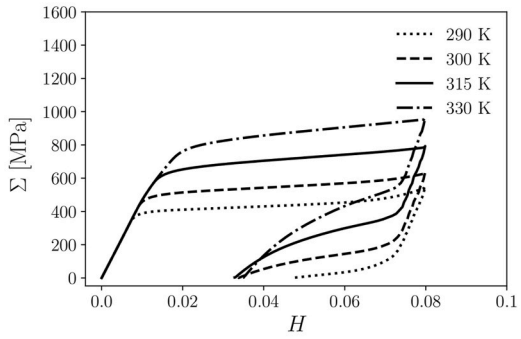

(a) Isothermal stress–strain plots for a solution heat-treated $Ni_{50.9}Ti$ (at.%) polycrystal at temperatures, T = 290, 300, 315, and 330 K. H stands for the average logarithmic strain in the direction of loading.

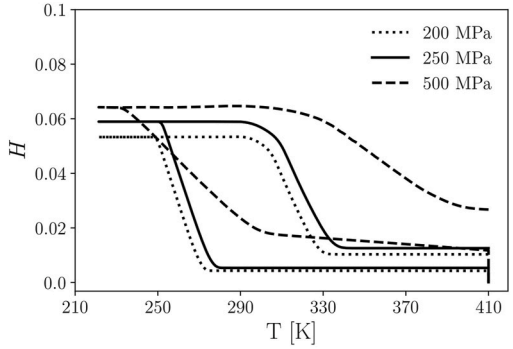

(b) Isobaric strain–temperature plots for an initially stress-free solution heat-treated $Ni_{50.9}Ti$ (at.%) polycrystal subjected to a thermal cycle under bias stress levels Σ = 400, 500, and 600 MPa.

Fig. 2. Isothermal mechanical and isobaric thermal loading simulations of polycrystalline NiTi.

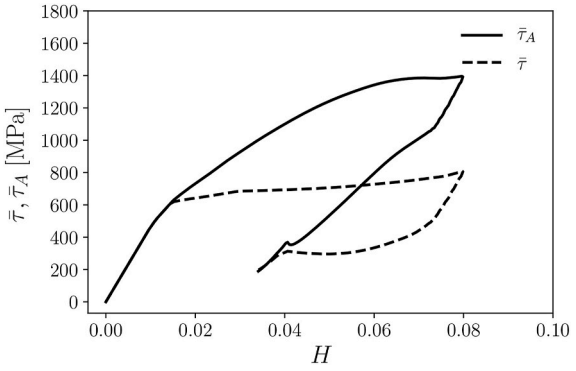

Fig. 3. Von Mises type values of Kirchhoff stress, $\bar{\tau}$, and local stress at the austenite phase, $\bar{\tau}_A$, at an integration point in the polycrystal vs average logarithmic strain at the direction of loading for the superelastic simulation at $T = 315$ K depicted in Fig. 2a.

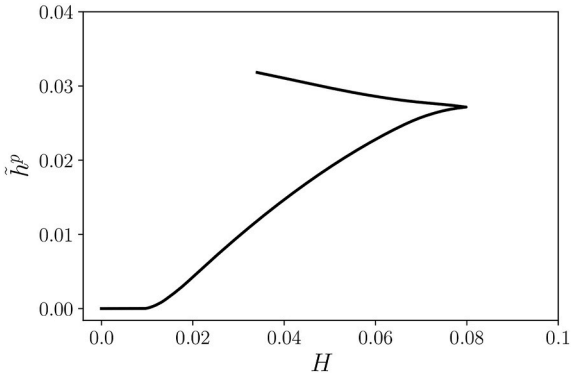

Fig. 4. Effective plastic strain at an integration point in the polycrystal vs average logarithmic strain at the direction of loading for the superelastic simulation at $T = 315$ K depicted in Fig. 2a.

all applied bias load levels. Both mechanical and thermal loading rates are assumed sufficiently slow with respect to the time rate of heat transfer by conduction/convection.

6.1.1. Uniaxial isothermal superelastic loading & isobaric loading

Polycrystalline constraints induce inhomogeneous phase transformation and plastic deformation resulting in stress–strain curves

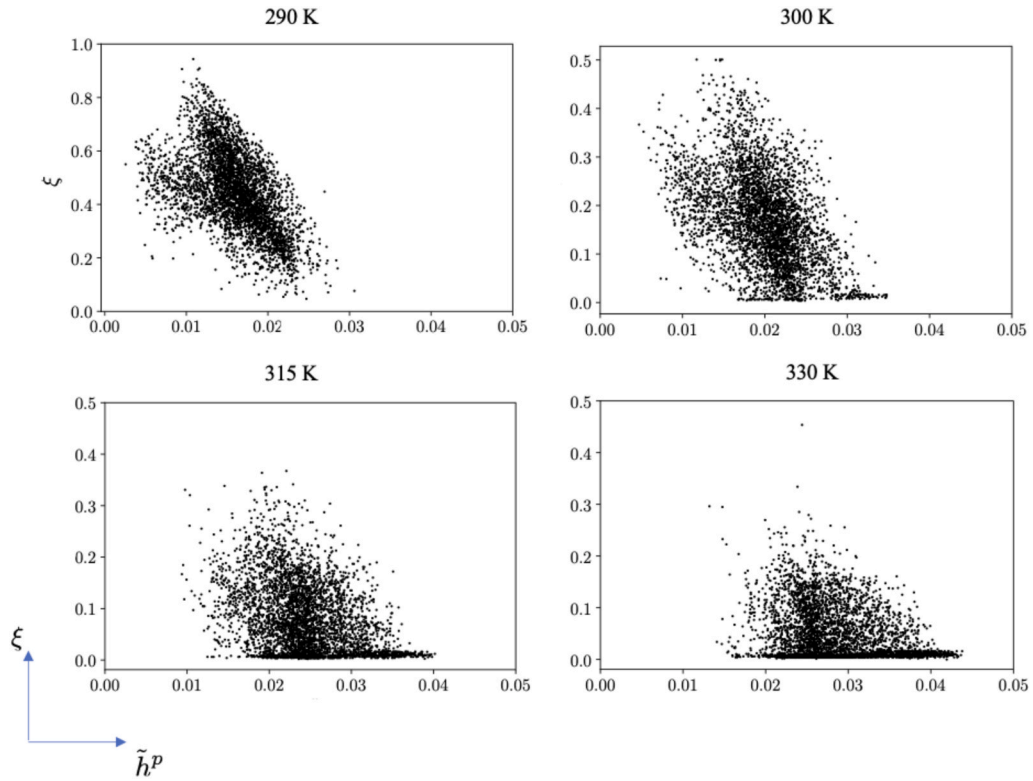

Fig. 5. Local martensite volume fraction vs local effective plastic strain at the end of unloading at all integration points for the superelastic simulations depicted in Fig. 2a. Note that the ξ-axis range in the subplot corresponding to 290 K is different from the corresponding range in the other subplots.

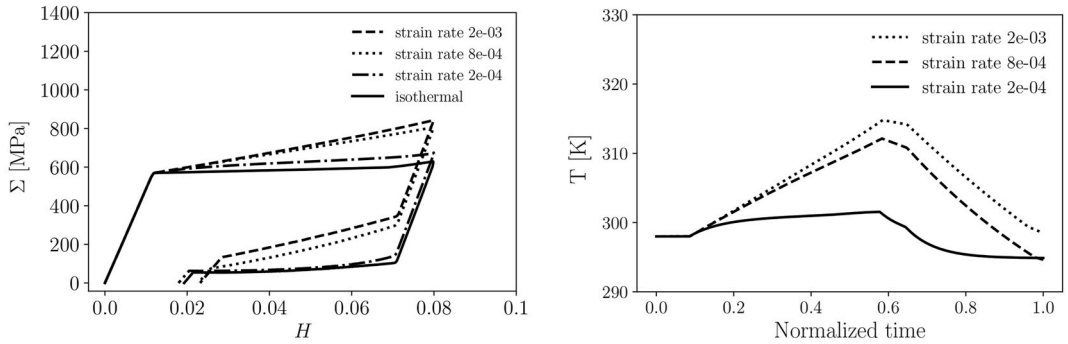

(a) Superelastic response for strain rates $2{\cdot}10^{-4}$, $8{\cdot}10^{-4}$, and $2 \cdot 10^{-3}$.

(b) Temperature evolution for the simulations depicted in (a).

Fig. 6. Latent-heat effects on the deformation response of an NiTi single crystal. The thermal boundary conditions correspond to heat convection in air.

that display more rounded (smooth) transitions and hardening than their single crystal counterparts (Fig. 2). The higher the temperature in the superelastic simulations, the higher the required load level for initiation/completion of macroscopic forward/reverse phase transformation. Similarly, the higher the bias load level in the isobaric simulations, the higher the temperature at initiation/completion of macroscopic forward/reverse phase transformation (Clapeyron slopes). Moreover, the higher the bias load levels, the higher the maximum macroscopic strain attained, up to a saturation value. Such a load dependence on the bias load levels has been reported in literature and it is attributed to the grain and loading orientation alignment; grains that are not favorably oriented require higher loads for attaining the same levels of transformation and plastic deformation as compared to the favorably oriented ones. Furthermore, the higher the bias load level, evidently the higher the irrecoverable deformation, *i.e.*, the induced plastic deformation.

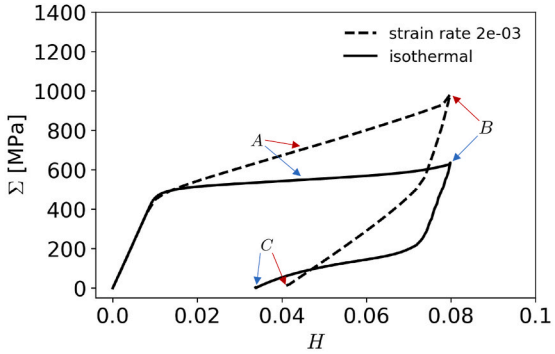

(a) Superelastic response for the isothermal case and for $2 \cdot 10^{-3}$ strain rate.

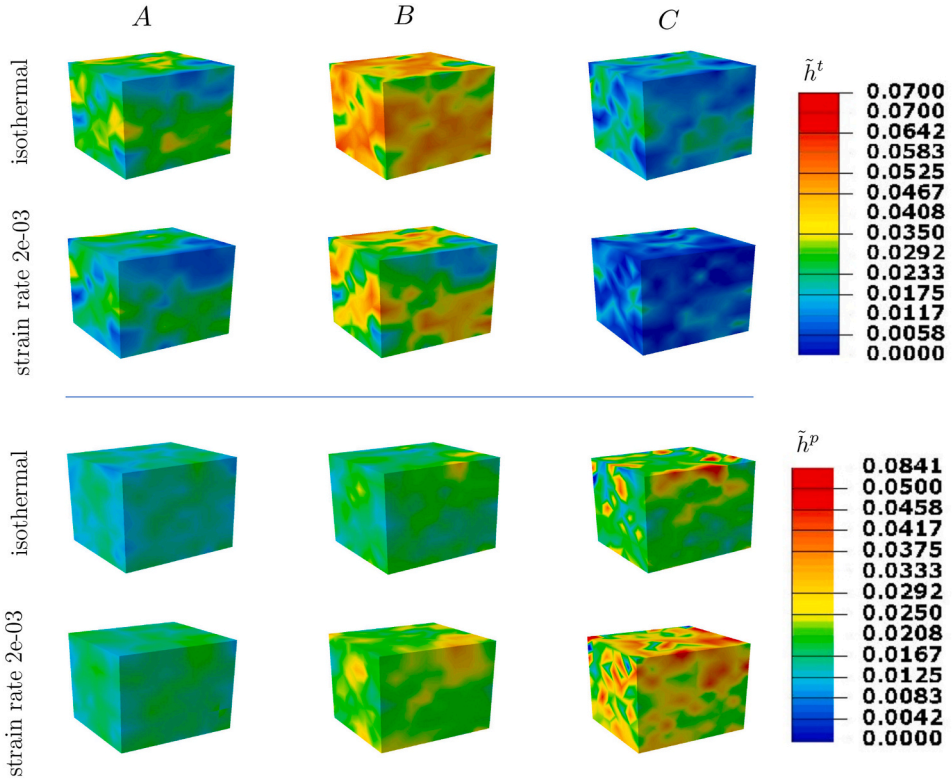

(b) Transformation and plastic effective strain contours at the instances denoted with the capital letters A, B, and C on the stress–strain curves in (a).

Fig. 7. Latent-heat effects on the deformation response of an NiTi polycrystal. The thermal boundary conditions correspond to heat convection in air.

6.1.2. Interplay between transformation and plastic deformation

The contribution of the deformation incompatibility at the austenite–martensite interfaces, which is accounted for by the mean-field micromechanics evaluation of the internal stress $\boldsymbol{\tau}_A$, in plastic deformation is depicted in Fig. 3 in which the von Mises type values of $\boldsymbol{\tau}_A$ and $\boldsymbol{\tau}$ at an integration point in one of the finite elements are plotted vs the average logarithmic strain H; the von Mises type value of a stress tensor $\boldsymbol{a}$ is defined as $\bar{a} = \sqrt{3/2(\boldsymbol{a}' : \boldsymbol{a}')}$, where $\boldsymbol{a}' = \boldsymbol{a} - \frac{1}{3}\mathrm{tr}(\boldsymbol{a})\boldsymbol{a}$ is the deviatoric stress tensor. It is clearly seen that $\bar{\boldsymbol{\tau}}_A$

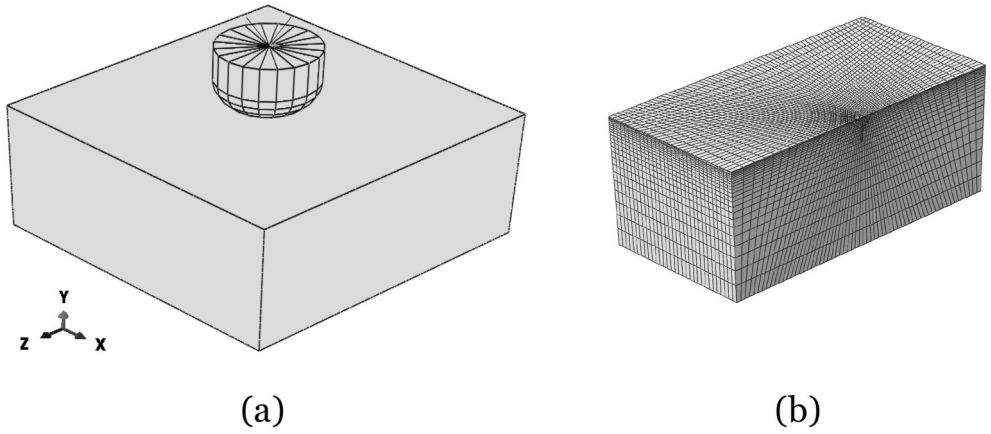

Fig. 8. (a) Indentation geometry; (b) The 3D finite element mesh discretization of the NiTi crystal block (half of the geometry is shown).

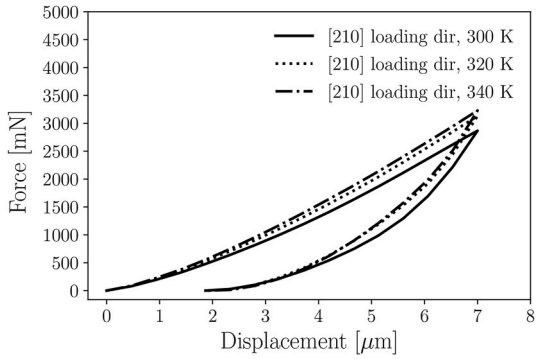

Fig. 9. Reaction force vs displacement of the indenter tip for isothermal simulations at 300, 320, and 340 K. The indentation direction is parallel to the [210] crystallographic direction.

rises to considerably higher values than $\dot{\tau}$ favoring dislocation slip activity.

In Fig. 4, it is shown that plastic deformation may be observed locally even during unloading despite the strain hardening experienced during loading, which should be attributed to the strong interactions among the grains, load shedding due to the accumulation of plastic deformation, and to the increase of the volume fraction of austenite $1-\xi$–see the driving force for plastic deformation given in eqn. (17). Furthermore, as it can be seen in the scatter plots presented in Fig. 5, in which the local martensite volume fraction is plotted vs the local effective plastic strain at the end of unloading at all integration points for the superelastic simulations depicted in Fig. 2a, the volume fraction of residual martensite due to incomplete transformation decreases with increasing temperature in accordance with the Clapeyron slopes observed experimentally. The scatter of the martensite volume fraction values is attributed to the interactions among the grains and load shedding due to phase transformation and plastic deformation. Regarding the latter, a rather weak correlation between residual martensite and plastic deformation is observed; the higher the local plastic deformation, the lower the residual martensite.

6.2. Latent-heat effects

Uniaxial loading simulations are performed at different loading rates to assess the model's ability to capture the rate-dependence on the NiTi deformation response associated with latent heat effects, *i.e.*, phase-transformation-induced heat generation/absorption. The thermal boundary conditions correspond to heat flux q due to convection in air of the form $\mathrm{q} = h\,(T - T_s)\mathrm{n}$, where h stands for the film coefficient, T_s is the sink temperature, and n is the outward unit normal to the deformed boundary. In the calculations, $h = 12$ W/(m^{2}K), which is standard for air, and $T_s = 298$ K. The thermal conductivity is assumed constant, equal to $k = (k_A + k_M)/2$ and the following approximation is adopted for the finite strain formulation $\nabla_x \cdot \left(J^{-1}\mathbf{F}k\mathbf{I}\mathbf{F}^T\nabla_x T\right) \approx k\nabla_x \cdot \nabla_x T$ since `Abaqus/Explicit®` only allows input of a single scalar value for the thermal conductivity (Thamburaja and Anand, 2003).

In Fig. 6a, the resulting superelastic stress–strain curves for three strain rates equal to $2\cdot10^{-4}$, $8\cdot10^{-4}$, and $2\cdot10^{-3}$ of single crystal loaded in the [211] direction are shown. The hysteresis loop corresponding to the lowest strain rate is very similar to that obtained from the isothermal calculation. The higher the loading rate, the steeper the inelastic response, *i.e.*, the steeper the slopes of

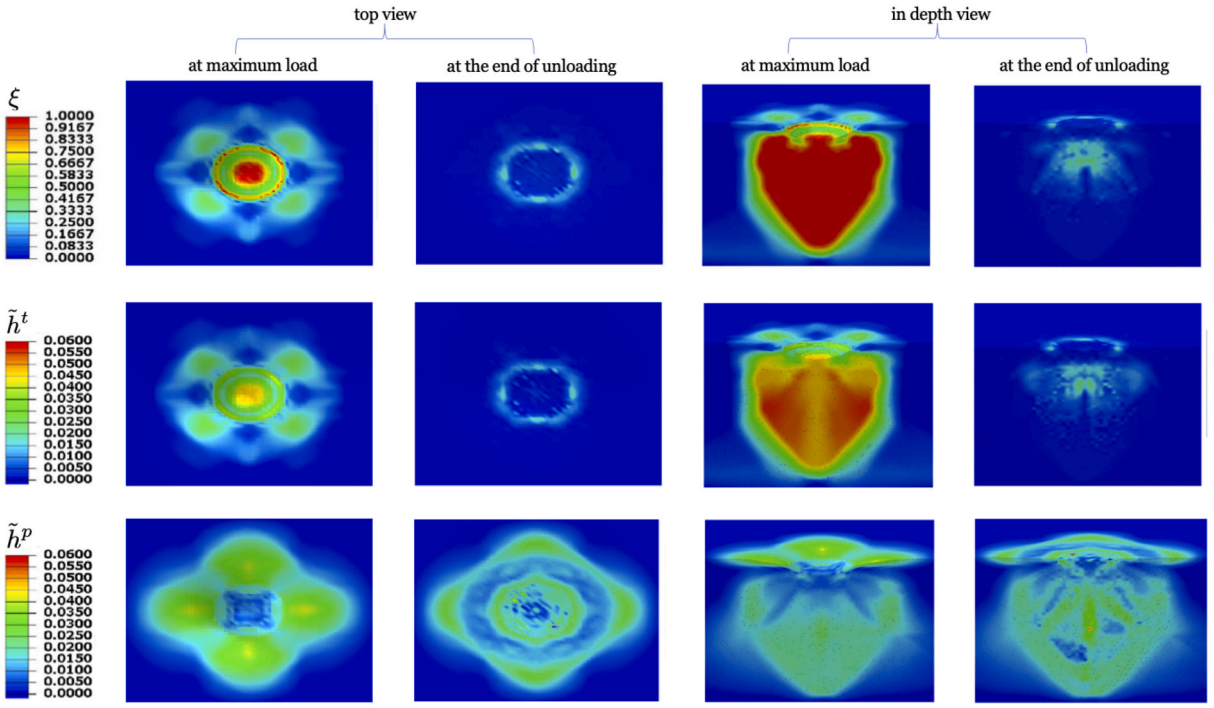

Fig. 10. Contour plots of the martensite volume fraction, effective transformation, and effective plastic strain profiles on the block's surface and on a cross section (in-depth direction) at the end of loading and the end of unloading. The indentation direction is parallel to the [010] crystallographic direction.

stress–strain curves during transformation/plastic deformation. The resulting response is the outcome of the interplay between the rate of heat generation/absorption during transformation, which influences the load required for phase transformation due to the Clapeyron slopes, and the rate of heat transfer by conduction/convection. The heat generated due to plastic deformation plays a minor role. During loading, the temperature of the material increases due to heat absorption induced from forward phase transformation and plastic deformation despite heat convection in air, which prevails during elastic unloading decreasing the temperature. During reverse phase transformation, the rate of cooling increases due to combined heat convection and transformation-induced heat absorption; it is even possible that the temperature may drop below the ambient temperature depending on the loading rate.

In Fig. 7a, the stress–strain curve obtained from uniaxial loading of the $8 \times 8 \times 8$ cube assembly of brick elements (Section 6.1.1) at $2 \cdot 10^{-3}$ strain rate is shown together with the corresponding stress–strain curve from the isothermal simulation. Similarly to the single crystal simulations, the thermomechanical coupling results in steeper slopes of stress–strain curves during transformation/plastic deformation. Transformation and plastic effective strain contours are presented in Fig. 7b at the instances denoted with the capital letters *A*, *B*, and *C* on the stress–strain curves in Fig. 7a. Point *A* is midway during the two plateaus at the same average logarithmic strain *H* for both curves, point *B* is at the end of loading (again at same strain *H* for both curves), and point *C* corresponds to the end of unloading. As shown in the figure, the strain distributions are non-homogeneous due to the distribution of grain orientations. At the same average inelastic strain, the distributions of effective transformation and plastic strains are different for the two simulations. The transformation strains at a material point are in general higher for the isothermal case compared to the $2 \cdot 10^{-3}$ strain-rate case while the plastic strains are lower. This response is attributed to the raise of temperature due to latent heat effects in the latter case, which influences the load required for phase transformation due to the Clapeyron slopes. The resulting increase in load for a certain martensite volume fraction to be attained, which is non-uniform due to the grain and loading orientation alignment and the induced latent heat effects, increases in turn the plastic deformation that can be induced at that martensite volume fraction.

6.3. *Microindentation of a single crystal*

In this section, microindentation simulations of a single NiTi crystal are presented in order to further demonstrate the efficiency and robustness of the numerical implementation of the model. The 3D finite element model, shown in Fig. 8, consists of (i) a single crystal block of dimensions $100 \times 100 \times 60$ μm discretized by a set of approximately 350,000 brick (C3D8) elements, and (ii) an indenter tip modeled as a rigid body with a hemispherical tip of a 15 μm radius. Displacement boundary conditions in the *y*-direction (indentation direction) are imposed on a reference node (placed at the center of the indenter), which is tied rigidly to the entire surface of the indenter. The top surface of the block is free to move while the bottom surface is constrained along the *y*-direction. Surface-to-surface contact definition is used to avoid any concentrated force buildup at individual nodes at initial point of contact. The friction coefficient between the block and the indenter is taken as 0.1.

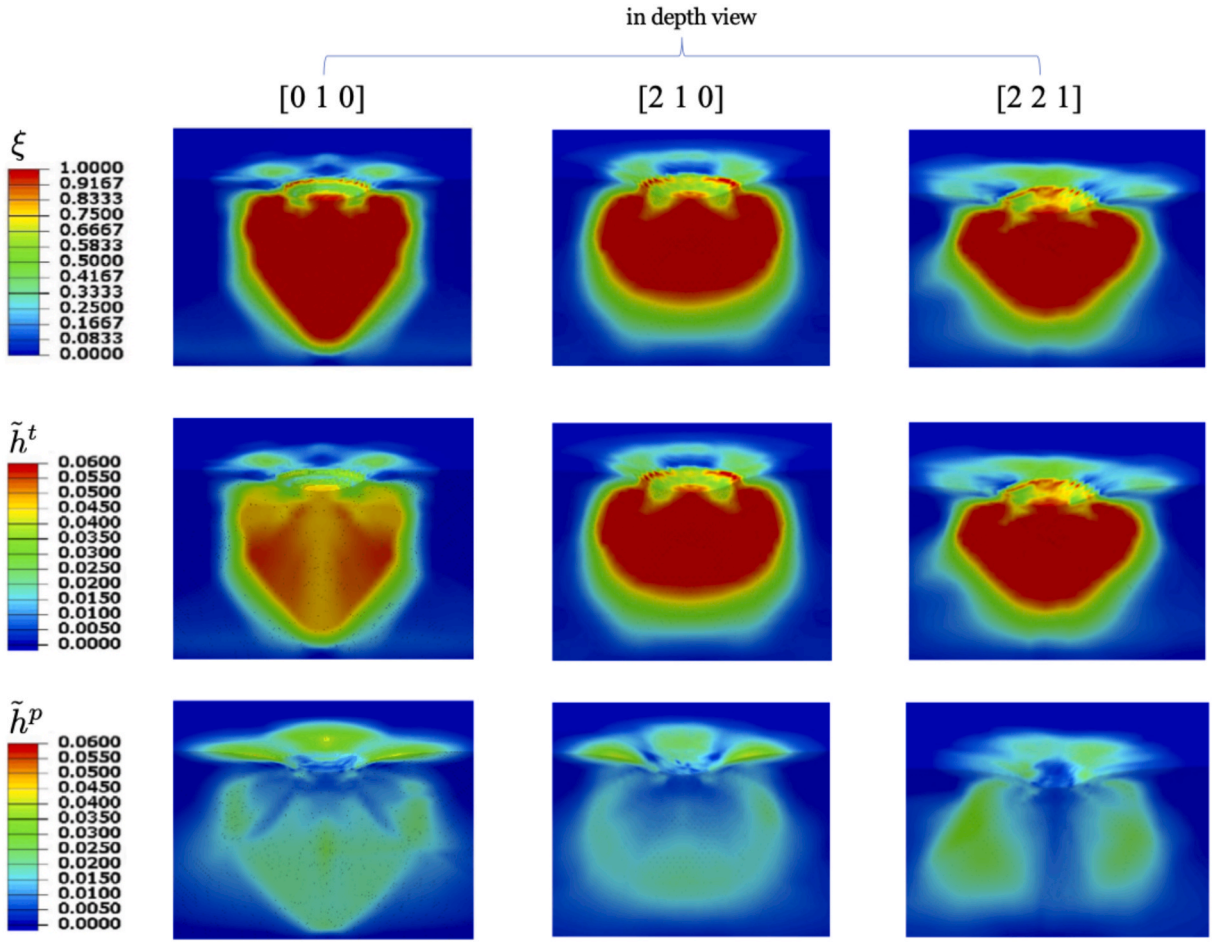

Fig. 11. Contour plots of the martensite volume fraction, effective transformation, and effective plastic strain profiles on the block's cross section (in-depth direction) at the end of loading for simulations in which the crystals are oriented such that the [010], [210], and [211] directions are parallel to the indentation direction.

The simulation results presented in Fig. 9 are for an indentation direction that corresponds to the [010] crystallographic direction in the block. The indenter's displacement vs the total reaction force exerted by the slave surface on the indenter are shown for isothermal simulations at 300, 320, and 340 K. The higher the temperature, the higher the load required for phase transformation/TRIP and, thus, the stiffer the material response. The simulated contour plots of the martensite volume fraction, effective transformation, and effective plastic strain profiles on the block's surface and on a cross section (in-depth direction) at the end of loading and the end of unloading are depicted in Fig. 10 for the simulation at 300 K. A four-fold symmetry of the distributions is shown. The contour plots in the in depth direction are compared with corresponding ones from simulations in which the indentation directions correspond to the [210] and [211] crystallographic directions in Fig. 11. It should be noted that the differences depicted in the figure are even more pronounced if, instead of effective values, individual components of the strain tensors and volume fractions of individual HPVs were plotted.

7. Summary

A subgrannular finite strain constitutive model for the thermomechanically-coupled, deformation response of NiTi under multi-axial loading has been proposed. The inelastic mechanisms included are (*i*) the reversible phase transformation of austenite to habit plane variants of martensite, and (*ii*) dislocation slipping in austenite. Interactions between transformation and plastic deformation are accounted for by a mean-field micromechanics evaluation of the internal stress raise due to deformation incompatibility at the austenite–martensite interfaces. This physics-based description of TRIP at the constitutive response level in a finite strain formalism that further accounts for rate effects induced by thermomechanical coupling (latent heat effects) differentiates the proposed model from available ones in literature. The evolution equations for the inelastic mechanisms are rate-dependent based on the Eulerian strain and its corotational objective rate. The finite strain formalism provides a robust framework to capture large rotations of material elements and surface roughening due to finite deformation observed in the simulations performed and examine complex geometries and loading

conditions, such as indentation.

Credit author statement

Md Afzal Hossain: Investigation, Writing–Original Draft Preparation. Theocharis Baxevanis: Conceptualization, Writing–Reviewing and Editing

Declaration of competing interest

The authors declare that they have no known competing financial interests or personal relationships that could have appeared to influence the work reported in this paper.

Acknowledgements

This study was supported by the National Science Foundation under Grant no. CMMI-1917441. The authors acknowledge the Research Computing Data Core (RCDC) at the University of Houston for the supercomputing resources made available for conducting the research reported in this paper.

A. Balance Laws

A.1. Balance of energy

Postulating the existence of a state function, the specific internal energy u (taken per unit volume), the first law of thermodynamics is written in local form as

$$\dot{u} = \boldsymbol{\sigma} : \dot{\boldsymbol{e}} - \nabla \cdot \mathrm{q} + r, \tag{A.1}$$

where q and r denote the heat flux at the referential state and heat supply per unit volume of the reference configuration, respectively, and σ denotes the Cauchy stress tensor.

A.2. Entropy Imbalance

Postulating the existence of specific entropy s, the second law of thermodynamics is stated as

$$\dot{s} + \frac{1}{T}\nabla \cdot \mathrm{q} - \frac{1}{T^2}\mathrm{q} \cdot \nabla T - \frac{r}{T} \geq 0, \tag{A.2}$$

which reduces to the strong form known as Clausius-Planck inequality

$$\dot{s} + \frac{1}{T}\nabla \cdot \mathrm{q} - \frac{r}{T} \geq 0, \tag{A.3}$$

or in terms of dissipation, D,

$$D = \dot{s}T + \nabla \cdot \mathrm{q} - r \geq 0, \tag{A.4}$$

where T stands for the absolute temperature.

Introducing the Helmholtz free energy per unit volume

$$\Phi = u - sT, \tag{A.5}$$

and in view of (A.1), (A.4) takes the following form

$$D = \boldsymbol{\sigma} : \dot{\boldsymbol{e}} - \dot{\Phi} - \dot{T}s \geq 0 \tag{A.6}$$

B. Crystallographic data for the 24 martensite HPVs in NiTi

The crystallographic data for the 24 martensite HPVs in NiTi is presented in Table 2.

Table 2
Crystallographic data for the 24 martensite HPVs in NiTi.

HPVs	Habit plane normal, l^α			Transformation direction, d^α		
1	0.8889	0.4044	0.21252	0.4114	0.4981	0.7633
2	0.4044	0.8889	0.2152	0.4981	0.4114	0.7633
3	0.8889	0.4044	0.2152	0.4114	0.4981	0.7633
4	0.4044	0.8889	0.2152	0.4981	0.4114	0.7633
5	0.8889	0.4044	0.2152	0.4114	0.4981	0.7633
6	0.4044	0.8889	0.2152	0.4981	0.4114	0.7633
7	0.8889	0.4044	0.2152	0.4114	0.4981	0.7633
8	0.4044	0.8889	0.2152	0.4981	0.4114	0.7633
9	0.2152	0.8889	0.4044	0.7633	0.4114	0.4981
10	0.2152	0.8889	0.4044	0.7633	0.4114	0.4981
11	0.2152	0.4044	0.8889	0.7633	0.4981	0.4114
12	0.2152	0.4044	0.8889	0.7633	0.4981	0.4114
13	0.2152	0.8889	0.4044	0.7633	0.4114	0.4981
14	0.2152	−0.8889	0.4044	−0.7633	0.4114	0.4981
15	0.2152	0.4044	−0.8889	0.7633	0.4981	0.4114
16	0.2152	−0.4044	0.8889	0.7633	−0.4981	−0.4114
17	0.8889	−0.2152	0.4044	−0.4114	−0.7633	0.4981
18	−0.8889	−0.2152	−0.4044	0.4114	−0.7633	−0.4981
19	0.4044	0.2152	0.8889	0.4981	0.7633	−0.4114
20	−0.4044	0.2152	−0.8889	−0.4981	0.7633	0.4114
21	0.8889	0.2152	−0.4044	−0.4114	0.7633	−0.4981
22	−0.8889	0.2152	0.4044	0.4114	0.7633	0.4981
23	−0.4044	−0.2152	0.8889	−0.4981	−0.7663	−0.4114
24	0.4044	−0.2152	−0.8889	0.4981	−0.7633	0.4114

C. Optimization of the model parameters

The least-square fitting of the set of model parameters $\boldsymbol{x} = \{{}^c_f f_t, {}^c_r f_t, {}^c_A f^r_p\ (r = 1,2,3), {}_A H_p, J_t\}$ is based on minimizing the objective function

$$\mathcal{Q}(\boldsymbol{x}) = \sum_\beta \sum_\alpha \left| \Sigma^\beta_\alpha(\boldsymbol{x}) - {}_e\Sigma^\beta_\alpha \right|^2 \tag{C.1}$$

where ${}_e\Sigma^\beta_\alpha$ are the experimental stress values that correspond to an α_{th}-strain value from the experimentally obtained stress–strain curve from a uniaxial compression along the β_{th}-crystallographic direction, and Σ^β_α are the corresponding simulated values.

The initial guesses for the parameter values were defined as follows. The initial values ${}^c_f f_t = 2.0$ MPa and ${}^c_r f_t = 20$ MPa were determined by matching the stress at the onset of the forward and reverse transformation from the room-temperature compressive stress–strain experimental data for [2 1 0] oriented single crystals, reported in Gall et al. (2002), that show little plastic deformation. The initial guesses for the critical forces for the slip families were based on the work of Chowdhury and Sehitoglu (2017), ${}^c_A f^1_p = 750$ MPa for the 6 slip-system family $\langle 100\rangle\{001\}$, ${}^c_A f^2_p = 600$ MPa for the 6 slip-system family $\langle 100\rangle\{011\}$, and ${}^c_A f^3_p = 500$ MPa for the 12 slip-system family $\langle 110\rangle\left\{\bar{1}11\right\}$. The initial guesses for the hardening parameters, ${}_A H_p$, and J_t, were arbitrary chosen.

Note that a Bayesian calibration of the model parameters has been performed in Honarmandi et al. (2021).

References

Anand, L., Gurtin, M.E., 2003. Thermal effects in the superelasticity of crystalline shape-memory materials. J. Mech. Phys. Solid. 51 (6), 1015–1058.

Barbarino, S., Flores, E.S., Ajaj, R.M., Dayyani, I., Friswell, M.I., 2014. A review on shape memory alloys with applications to morphing aircraft. Smart Mater. Struct. 23 (6), 063001.

Benafan, O., Noebe, R., Padula II, S., Brown, D., Vogel, S., Vaidyanathan, R., 2014. Thermomechanical cycling of a NiTi shape memory alloy–macroscopic response and microstructural evolution. Int. J. Plast. 56, 99–118.

Benafan, O., Noebe, R., Padula Ii, S., Garg, A., Clausen, B., Vogel, S., Vaidyanathan, R., 2013. Temperature dependent deformation of the B2 austenite phase of a NiTi shape memory alloy. Int. J. Plast. 51, 103–121.

Beyerlein, I., Tomé, C., 2008. A dislocation-based constitutive law for pure Zr including temperature effects. Int. J. Plast. 24 (5), 867–895.

Bornert, M., Bretheau, T., Gilormini, P., 2001. Homogénéisation en mécanique des matériaux 1. Matériaux aléatoires élastiques et milieux périodiques. Hermes Sciences Europe Ltd.

Brill, T., Mittelbach, S., Assmus, W., Mullner, M., Luthi, B., 1991. Elastic properties of NiTi. J. Phys. Condens. Matter 3 (48), 9621.

Brinson, L.C., Schmidt, I., Lammering, R., 2004. Stress-induced transformation behavior of a polycrystalline NiTi shape memory alloy: micro and macromechanical investigations via in situ optical microscopy. J. Mech. Phys. Solid. 52 (7), 1549–1571.

Bruhns, O., Xiao, H., Meyers, A., 2003. Some basic issues in traditional eulerian formulations of finite elastoplasticity. Int. J. Plast. 19 (11), 2007–2026.

Cherkaoui, M., Berveiller, M., Sabar, H., 1998. Micromechanical modeling of martensitic transformation induced plasticity (TRIP) in austenitic single crystals. Int. J. Plast. 14 (7), 597–626.
Chowdhury, P., Sehitoglu, H., 2017. A revisit to atomistic rationale for slip in shape memory alloys. Prog. Mater. Sci. 85, 1–42.
Christ, S., Reese, S., 2008. Finite-element modelling of shape memory alloys–a comparison between small-strain and large-strain formulations. Mater. Sci. Eng., A 481–482, 343–346.
Chumlyakov, Y.I., Kireeva, I., Korotaev, A., Litvinova, E., Zuev, Y.L., 1996. Mechanisms of plastic deformation, hardening, and fracture in single crystals of nitrogen-containing austenitic stainless steels. Russ. Phys. J. 39 (3), 189–210.
Coleman, B., Gurtin, M., 1967. Thermodynamics with internal state variables. J. Chem. Phys. 47 (2), 597–613.
Cormeau, I., 1975. Numerical stability in quasi-static elasto/visco-plasticity. Int. J. Numer. Methods Eng. 9 (1), 109–127.
Darijani, H., Naghdabadi, R., 2010. Constitutive modeling of solids at finite deformation using a second-order stress–strain relation. Int. J. Eng. Sci. 48 (2), 223–236.
Delville, R., Kasinathan, S., Zhang, Z., Humbeeck, J.V., James, R.D., Schryvers, D., 2010. Transmission electron microscopy study of phase compatibility in low hysteresis shape memory alloys. Phil. Mag. 90 (1–4), 177–195.
Delville, R., Malard, B., Pilch, J., Sittner, P., Schryvers, D., 2011. Transmission electron microscopy investigation of dislocation slip during superelastic cycling of Ni–Ti wires. Int. J. Plast. 27 (2), 282–297.
Dhala, S., Mishra, S., Tewari, A., Alankar, A., 2019. Modeling of finite deformation of pseudoelastic NiTi shape memory alloy considering various inelasticity mechanisms. Int. J. Plast. 115, 216–237.
Eggeler, G., Hornbogen, E., Yawny, A., Heckmann, A., Wagner, M., 2004. Structural and functional fatigue of NiTi shape memory alloys. Mater. Sci. Eng. 378 (1), 24–33.
Ezaz, T., Wang, J., Sehitoglu, H., Maier, H., 2013. Plastic deformation of NiTi shape memory alloys. Acta Mater. 61 (1), 67–78.
Gall, K., Dunn, M.L., Liu, Y., Labossiere, P., Sehitoglu, H., Chumlyakov, Y.I., 2002. Micro and macro deformation of single crystal NiTi. J. Eng. Mater. Technol. 124 (2), 238–245.
Gall, K., Lim, T.J., McDowell, D.L., Sehitoglu, H., Chumlyakov, Y.I., 2000. The role of intergranular constraint on the stress-induced martensitic transformation in textured polycrystalline NiTi. Int. J. Plast. 16 (10–11), 1189–1214.
Gall, K., Maier, H., 2002. Cyclic deformation mechanisms in precipitated NiTi shape memory alloys. Acta Mater. 50 (18), 4643–4657.
Gall, K., Sehitoglu, H., 1999. The role of texture in tension–compression asymmetry in polycrystalline niti. Int. J. Plast. 15 (1), 69–92.
Gall, K., Sehitoglu, H., Anderson, R., Karaman, I., Chumlyakov, Y.I., Kireeva, I.V., 2001. On the mechanical behavior of single crystal NiTi shape memory alloys and related polycrystalline phenomenon. Mater. Sci. Eng., A 317 (1–2), 85–92.
Gao, X., Huang, M., Brinson, L.C., 2000. A multivariant micromechanical model for SMAs Part 1. Crystallographic issues for single crystal model. Int. J. Plast. 16 (10–11), 1345–1369.
Hamilton, R., Sehitoglu, H., Chumlyakov, Y., Maier, H., 2004. Stress dependence of the hysteresis in single crystal NiTi alloys. Acta Mater. 52 (11), 3383–3402.
Hane, K.F., Shield, T., 1999. Microstructure in the cubic to monoclinic transition in titanium–nickel shape memory alloys. Acta Mater. 47 (9), 2603–2617.
He, Y.J., Sun, Q., 2011. On non-monotonic rate dependence of stress hysteresis of superelastic shape memory alloy bars. Int. J. Solid Struct. 48 (11–12), 1688–1695.
Hencky, H., 1928. Uber die form des elastizitatsgesetzes bei ideal elastischen stoffen. Zeit. Tech. Phys. 9, 215–220.
Honarmandi, P., Hossain, M., Arroyave, R., Baxevani, T., 2021. A top-down characterization of NiTi single crystal inelastic properties within confidence bounds through bayesian inference. Shape Mem. Super. https://doi.org/10.1007/s40830-021-00311-8.
Huang, M., Gao, X., Brinson, L., 2000. A multivariant micromechanical model for SMAs. Part 2: polycrystal model. Int. J. Plast. 16 (10–11), 1371–1390.
Jani, J.M., Leary, M., Subic, A., Gibson, M.A., 2014. A review of shape memory alloy research, applications and opportunities. Mater. Des. 56, 1078–1113.
Kang, G., Kan, Q., Qian, L., Liu, Y., 2009. Ratchetting deformation of super-elastic and shape-memory NiTi alloys. Mech. Mater. 41 (2), 139–153.
Kang, G., Kan, Q., Yu, C., Song, D., Liu, Y., 2012. Whole-life transformation ratchetting and fatigue of super-elastic NiTi Alloy under uniaxial stress-controlled cyclic loading. Mater. Sci. Eng., A 535, 228–234.
Kröner, E., 1961. Zur plastischen verformung des vielkristalls. Acta Metall. 9 (2), 155–161.
Lagoudas, D. (Ed.), 2008. Shape Memory Alloys: Modelling and Enginnering Applications. Springer, New-York.
Leo, P.H., Shield, T.W., Bruno, O.P., 1993. Transient heat transfer effects on the pseudoelastic behavior of shape-memory wires. Acta Metall. Mater. 41 (8), 2477–2485.
Malvern, L., 1998. Introduction to the Mechanics of Continuous Medium. Prentice-Hall, Inc., Englewood Cliffs.
Manchiraju, S., Anderson, P.M., 2010. Coupling between martensitic phase transformations and plasticity: a microstructure-based finite element model. Int. J. Plast. 26 (10), 1508–1526.
Manchiraju, S., Gaydosh, D., Benafan, O., Noebe, R., Vaidyanathan, R., Anderson, P.M., 2011. Thermal cycling and isothermal deformation response of polycrystalline NiTi: simulations vs. experiment. Acta Mater. 59 (13), 5238–5249.
Matsumoto, O., Miyazaki, S., Otsuka, K., Tamura, H., 1987. Crystallography of martensitic transformation in Ti–Ni single crystals. Acta Metall. 35 (8), 2137–2144.
McCormick, P., Liu, Y., Miyazaki, S., 1993. Intrinsic thermal-mechanical behaviour associated with the stress-induced martensitic transformation in NiTi. Mater. Sci. Eng., A 167 (1–2), 51–56.
Miyazaki, S., 1990. Engineering Aspects of Shape Memory Alloys. Butterworth-Heinemann, London.
Miyazaki, S., Imai, T., Igo, Y., Otsuka, K., 1986. Effect of cyclic deformation on the pseudoelasticity characteristics of Ti-Ni alloys. Metallurgical transactions A 17 (1), 115–120.
Monroe, J., Gehring, D., Karaman, I., Arroyave, R., Brown, D.W., Clausen, B., 2016. Tailored thermal expansion alloys. Acta Mater. 102, 333–341.
Morgan, N., 2004. Medical shape memory alloy applications – the market and its products. Mater. Sci. Eng., A 378, 16–23.
Mori, T., Tanaka, K., 1973. Average stress in matrix and average elastic energy of materials with misfitting inclusions. Acta Metall. 21 (5), 571–574.
Morin, C., Moumni, Z., Zaki, W., 2011a. A constitutive model for shape memory alloys accounting for thermomechanical coupling. Int. J. Plast. 27 (5), 748–767.
Morin, C., Moumni, Z., Zaki, W., 2011b. Thermomechanical coupling in shape memory alloys under cyclic loadings: experimental analysis and constitutive modeling. Int. J. Plast. 27 (12), 1959–1980.
Morin, C., Moumni, Z., Zaki, W., 2011c. Thermomechanical coupling in shape memory alloys under cyclic loadings: experimental analysis and constitutive modeling. Int. J. Plast. 27, 1959–1980.
Müller, C., Bruhns, O., 2006. A thermodynamic finite-strain model for pseudoelastic shape memory alloys. Int. J. Plast. 22 (9), 1658–1682.
Nemat-Nasser, S., Guo, W.-G., 2006. Superelastic and cyclic response of NiTi SMA at various strain rates and temperatures. Mech. Mater. 38 (5–6), 463–474.
Norfleet, D., Sarosi, P., Manchiraju, S., Wagner, M.-X., Uchic, M., Anderson, P., Mills, M., 2009. Transformation-induced plasticity during pseudoelastic deformation in Ni–Ti microcrystals. Acta Mater. 57 (12), 3549–3561.
Otsuka, K., Ren, X., 2005. Physical metallurgy of ti–ni-based shape memory alloys. Prog. Mater. Sci. 50 (5), 511–678.
Otsuka, K., Wayman, C. (Eds.), 1999. Shape Memory Materials. Cambridge University Press, Cambridge.
Paranjape, H.M., Manchiraju, S., Anderson, P.M., 2016. A phase field–finite element approach to model the interaction between phase transformations and plasticity in shape memory alloys. Int. J. Plast. 80, 1–18.
Patoor, E., Eberhardt, A., Berveiller, M., 1996. Micromechanical modelling of superelasticity in shape memory alloys. J. Phys. IV France 6 (C1), 277–292.
Patoor, E., Lagoudas, D., Entchev, P., Brinson, L., Gao, X., 2006. Shape memory alloys. part i: general properties and modeling of single crystals. Mech. Mater. 38, 391–429.
Peirce, D., Shih, C.F., Needleman, A., 1984. A tangent modulus method for rate dependent solids. Comput. Struct. 18 (5), 875–887.
Pelton, A., Huang, G., Moine, P., Sinclair, R., 2012. Effects of thermal cycling on microstructure and properties in Nitinol. Mater. Sci. Eng., A 532, 130–138.
Pfetzing-Micklich, J., Ghisleni, R., Simon, T., Somsen, C., Michler, J., Eggeler, G., 2012. Orientation dependence of stress-induced phase transformation and dislocation plasticity in NiTi shape memory alloys on the micro scale. Mater. Sci. Eng., A 538, 265–271.
Prahlad, H., Chopra, I., 2003. Development of a strain-rate dependent model for uniaxial loading of SMA wires. J. Intell. Mater. Syst. Struct. 14 (14), 429–442.

Reese, S., Christ, D., 2008. Finite deformation pseudo-elasticity of shape memory alloys–constitutive modelling and finite element implementation. Int. J. Plast. 24 (3), 455–482.
Reinhardt, W., Dubey, R., 1995. Eulerian strain-rate as a rate of logarithmic strain. Mech. Res. Commun. 22 (2), 165–170.
Shaw, J., Kyriakides, S., 1995. Thermomechanical aspects of NiTi. J. Mech. Phys. Solid. 43 (8), 1243–1281.
Simo, J., Hughes, T., 1998. Computational Inelasticity. Springer-Verlag, Inc., New York.
Simon, T., Kröger, A., Somsen, C., Dlouhy, A., Eggeler, G., 2010. On the multiplication of dislocations during martensitic transformations in NiTi shape memory alloys. Acta Mater. 58 (5), 1850–1860.
Siredey, N., Patoor, E., Berveiller, M., Eberhardt, A., 1999. Constitutive equations for polycrystalline thermoelastic shape memory alloys.: Part I. Intragranular interactions and behavior of the grain. Int. J. Solid Struct. 36 (28), 4289–4315.
Song, D., Kang, G., Kan, Q., Yu, C., Zhang, C., 2014. Non-proportional multiaxial transformation ratchetting of super-elastic NiTi shape memory alloy: experimental observations. Mech. Mater. 70, 94–105.
Sun, L., Huang, W.M., Ding, Z., Zhao, Y., Wang, C.C., Purnawali, H., Tang, C., 2012. Stimulus-responsive shape memory materials: a review. Mater. Des. 33, 577–640.
Thamburaja, P., 2005. Constitutive equations for martensitic reorientation and detwinning in shape-memory alloys. J. Mech. Phys. Solid. 53 (4), 825–856.
Thamburaja, P., Anand, L., 2001. Polycrystalline shape-memory materials: effect of crystallographic texture. J. Mech. Phys. Solid. 49 (4), 709–737.
Thamburaja, P., Anand, L., 2002. Superelastic behavior in tension–torsion of an initially-textured Ti–Ni shape-memory alloy. Int. J. Plast. 18 (11), 1607–1617.
Thamburaja, P., Anand, L., 2003. Thermo-mechanically coupled superelastic response of initially-textured Ti-Ni sheet. Acta Mater. 51 (2), 325–338.
Thamburaja, P., Nikabdullah, N., 2009. A macroscopic constitutive model for shape-memory alloys: theory and finite-element simulations. Comput. Methods Appl. Mech. Eng. 198 (9–12), 1074–1086.
Wang, X., Xu, B., Yue, Z., 2008. Micromechanical modelling of the effect of plastic deformation on the mechanical behaviour in pseudoelastic shape memory alloys. Int. J. Plast. 24 (8), 1307–1332.
Xiao, H., Bruhns, O., Meyers, A., 1997. Logarithmic strain, logarithmic spin and logarithmic rate. Acta Mech. 124 (1–4), 89–105.
Xiao, H., Bruhns, O., Meyers, A., 2000. A consistent finite elastoplasticity theory combining additive and multiplicative decomposition of the stretching and the deformation gradient. Int. J. Plast. 16 (2), 143–177.
Xiao, H., Bruhns, O., Meyers, A., 2004. Explicit dual stress-strain and strain-stress relations of incompressible isotropic hyperelastic solids via deviatoric Hencky strain and Cauchy stress. Acta Mech. 168 (1–2), 21–33.
Xiao, H., Bruhns, O.T., Meyers, A., 1996. Logarithmic strain, logarithmic spin and logarithmic rate. Acta Mech. 124, 89–105.
Xiao, Y., Zeng, P., Lei, L., 2018. Micromechanical modeling on thermomechanical coupling of cyclically deformed superelastic NiTi shape memory alloy. Int. J. Plast. 107, 164–188.
Yin, H., He, Y., Sun, Q., 2014. Effect of deformation frequency on temperature and stress oscillations in cyclic phase transition of NiTi shape memory alloy. J. Mech. Phys. Solid. 67, 100–128.
Yin, H., Sun, Q., 2012. Temperature variation in NiTi shape memory alloy during cyclic phase transition. J. Mater. Eng. Perform. 21 (12), 2505–2508.
Yu, C., Kang, G., Kan, Q., 2015a. A micromechanical constitutive model for anisotropic cyclic deformation of super-elastic NiTi shape memory alloy single crystals. J. Mech. Phys. Solid. 82, 97–136.
Yu, C., Kang, G., Kan, Q., Zhu, Y., 2015b. Rate-dependent cyclic deformation of super-elastic NiTi shape memory alloy: thermo-mechanical coupled and physical mechanism-based constitutive model. Int. J. Plast. 72, 60–90.
Yu, C., Kang, G., Sun, Q., Fang, D., 2019. Modeling the martensite reorientation and resulting zero/negative thermal expansion of shape memory alloys. J. Mech. Phys. Solid. 127, 295–331.
Zaki, W., Moumni, Z., 2007. A 3D model of the cyclic thermomechanical behavior of shape memory alloys. J. Mech. Phys. Solid. 55 (11), 2427–2454.